

## Rising from the Ashes II: Can Bar Formation Lead to Abundance Bimodalities?

ANGUS BEANE,<sup>1</sup> JAMES W. JOHNSON,<sup>2</sup> VADIM SEMENOV,<sup>1</sup> LARS HERNQUIST,<sup>1</sup> VEDANT CHANDRA,<sup>1</sup> AND CHARLIE CONROY<sup>1</sup>

<sup>1</sup>*Center for Astrophysics | Harvard & Smithsonian, Cambridge, MA, USA*

<sup>2</sup>*The Observatories of the Carnegie Institution for Science, Pasadena, CA, USA*

### ABSTRACT

The Milky Way is known to host at least two modes in its present day distribution of Fe and  $\alpha$ -elements. The exact cause of this bimodality is disputed, but one class of explanations involves the merger between the Milky Way and a relatively massive satellite (Gaia-Sausage-Enceladus) at  $z \sim 2$ . However, reproducing this bimodality in simulations is not straightforward, with conflicting results on the prevalence, morphology, and mechanism behind multimodality. We present a case study of a galaxy in the Illustris TNG50 simulation which undergoes a sequence of starburst, brief quiescence, and then rejuvenation. After a minor post-processing step which boosts the  $[\alpha/\text{Fe}]$  of old star particles, we demonstrate that this galaxy hosts a strongly bimodal distribution in the  $[\alpha/\text{Fe}]\text{-}[\text{Fe}/\text{H}]$  plane. The high- and low- $\alpha$  sequences are neatly separated in time by the brief quiescent period. The quiescent period in this galaxy is not associated with a merger but by the formation of a bar followed by AGN activity. This galaxy indicates a novel scenario in which the  $\alpha$ -bimodality is caused by AGN-induced quenching triggered by the formation of the Milky Way's bar. We argue that the post-processing step can be interpreted as the TNG model underproducing star formation in the densest regions at high- $z$ .

**Keywords:** Classical Novae (251) — Ultraviolet astronomy(1736) — History of astronomy(1868) — Interdisciplinary astronomy(804)

### 1. INTRODUCTION

The stellar surface abundances of most elements retain the composition of their natal gas cloud. Therefore, the present-day distribution of stellar surface abundances encodes the chemical history of a galaxy's gas phase. Two elements have received particular interest in the Milky Way: Fe and  $\alpha$ -elements (elements produced through the  $\alpha$ -process, such as O and Mg). Fe is produced in both Type Ia and Type II SNe whereas  $\alpha$ -elements are produced predominantly through Type II SNe. Because these SNe occur on different timescales (10s of Myr after star formation for Type II, as compared to 100s of Myr to Gyrs for Type Ia), the ratio between  $\alpha$ -elements and Fe is expected to generally decrease with time.

Because of their separate formation channels, the two dimensional plane of  $[\alpha/\text{Fe}]\text{-}[\text{Fe}/\text{H}]$  has received considerable interest. In the Milky Way, there is a well-established bimodality with separate high- and low- $\alpha$  sequences (Gratton et al. 1996; Fuhrmann 1998, 2004; Reddy et al. 2006; Adibekyan et al. 2011, 2012; Bensby et al. 2014; Nidever et al. 2014; Hayden et al. 2020). This bimodal distribution is shown in the upper left panel of Figure 1.

There are essentially two approaches to explaining the bimodality. First, it is a result of internal secular processes that generate the bimodality through radial migration (Schönrich

& Binney 2009; Sharma et al. 2021; Chen et al. 2023) or clump formation (Clarke et al. 2019; Beraldo e Silva et al. 2020, 2021; Garver et al. 2023).

Second, the bimodality is generated through gas infall scenarios, either from specific gas accretion episodes from the intergalactic medium (Chiappini et al. 1997; Chiappini 2009; Grisoni et al. 2017; Spitoni et al. 2019), or through a more self-consistent collapse sequence of the circumgalactic medium driven through feedback (Khoperskov et al. 2021). Third and finally, the bimodality is generated through a merger process, either by enhancing the SFR of the Galaxy (Brook et al. 2004, 2005, 2007; Richard et al. 2010) or by supplying a relatively pristine gas supply that resets the metallicity of the Galaxy (Buck 2020; Ciucă et al. 2024). The fact that the Milky Way did undergo a merger with the Gaia-Sausage-Enceladus (GSE) satellite supports these scenarios (Belokurov et al. 2018; Helmi et al. 2018; Naidu et al. 2020; Chandra et al. 2024).

In Beane (2024) we argued for an alternate formation scenario of the bimodality, for which we provide further support in this work. In this scenario, the bimodality is formed through a brief quiescent period in the Galaxy's history. During this period, which lasted  $\sim 300$  Myr in that setup, two things happen. First, as the chemical evolution of the galaxy proceeds, fewer stars form. Second, because the SFR is lower,

$\alpha$ -element production drops and so the  $[\alpha/\text{Fe}]$  of the gas drops as well. This is conceptually similar to some variants of the two-phase infall scenarios which allow for a brief halt in the star formation rate (Spitoni et al. 2024, and references therein), though the quiescent period is much shorter in Beane (2024). The combination of these two effects is what leads to the valley in between the high- and low- $\alpha$  sequences.

In that work, we used idealized simulations of a galaxy merger that triggered a starburst which preceded the quiescent period. However, we argued that the merger aspect of that work was not necessary, but rather the quiescence. In this work, we study a subhalo from the Illustris TNG50 simulation which demonstrates this. This subhalo of interest (SoI) exhibits the sequence of events presented in Beane (2024) after a simple post-processing step which enhances the  $[\alpha/\text{Fe}]$  of old star particles. The SoI undergoes a brief quiescent period which neatly separates a high- and low- $\alpha$  sequence. However, instead of being preceded by a merger, the quenching is preceded by apparent bar-induced AGN activity. Therefore, this work serves as a verification that the scenario in Beane (2024) is possible in cosmological simulations and can occur in non-merger scenarios.

In Section 2 we discuss our selection technique which led to discovering the SoI, the observations we use for comparison, as well as a simple one zone chemical evolution model we use to justify our post-processing step. In Section 3 we present the main results which we discuss and interpret in Section 4. We conclude in Section 5.

## 2. METHODS

### 2.1. *IllustrisTNG Sample*

We have made use of the Illustris TNG50 simulation (Pillepich et al. 2019; Nelson et al. 2019), a cosmological simulation of a  $\sim 50 \text{ cMpc}$  box at high resolution ( $m_{\text{baryon}} \sim 8.5 \times 10^4 M_\odot$ ). It uses the gravito-magneto-hydrodynamics code AREPO (Springel 2010; Pakmor et al. 2016), along with the TNG model (Vogelsberger et al. 2013; Weinberger et al. 2017; Pillepich et al. 2018). This model includes several sub-grid processes: a wind generation model, chemical enrichment from supernovae and asymptotic giant branch stars, and thermal and kinetic feedback from AGN.

One piece of the TNG model of note for this work is the BH accretion and feedback method (Weinberger et al. 2017). The black hole accretion rate ( $\dot{M}_{\text{BH}}$ ) is computed using the local structure of the gas phase with the Bondi-Hoyle-Lyttleton formula (Hoyle & Lyttleton 1939; Bondi & Hoyle 1944; Bondi 1952), with a maximum of the Eddington accretion rate ( $\dot{M}_{\text{edd}}$ ). The model allows the BH to be either in a kinetic radio-mode or a thermal quasar-mode. If the Eddington ratio ( $\dot{M}_{\text{BH}}/\dot{M}_{\text{edd}}$ ) exceeds a threshold ( $\dot{M}_{\text{BH}}$ -dependent, but  $\sim 0.001 - 0.1$ ), the BH is in the quasar mode and injects a large amount of thermal energy into its surroundings.

Using the public catalog, we selected a sample of subhalos at  $z = 1.5$  (snapshot 40) according to the following criteria: (1) the subhalo is central (i.e., the most massive subhalo within its halo), and (2) the subhalo's stellar mass is between  $10^{10}$  and  $10^{10.5} M_\odot/\text{h}$ . There were a total of 168 subhalos that met both criteria. The chosen mass range is broadly consistent with the expected mass of the Milky Way at this redshift (van Dokkum et al. 2013). We chose to make our selection of galaxies at  $z = 1.5$  instead of at lower redshift because we wished to capture the *formation* of any multimodal structure. We did not want contamination by mergers at lower redshift which we know contribute very little to the Milky Way's disk stars (e.g., Bland-Hawthorn & Gerhard 2016).

We examined the abundance distribution in the  $[\text{Mg}/\text{Fe}]$ - $[\text{Fe}/\text{H}]$  plane of this sample of subhalos by eye. Not many subhalos had multimodal structure, and any structure that was present was relatively weak compared to that observed in the Milky Way. We then applied a post-processing to the  $[\text{Mg}/\text{Fe}]$  of stars by adding to each star particle a value of  $0.1 \times (t_{1.5} - t_{\text{form}})$ , where  $t_{1.5}$  is the age of the universe at  $z = 1.5$  ( $\sim 4.3 \text{ Gyr}$ ) and  $t_{\text{form}}$  is the formation time of each star particle. With this post-processing, we found that much more structure was generally present.

We show the abundance distributions (replicating Figure 1) of 16 random subhalos from our catalog, and the subhalo we selected, in Appendix B. Of these subhalos, some structure is present, but none have a strong bimodality as seen in the Milky Way. After the  $\alpha$ -enhancement, a few have strongly bimodal features (subject to interpretation): 172175, 178140, 193025.

We selected subhalo 172175 (the ID at snapshot 40) for its particular resemblance to the Milky Way. We then studied the main descendant of this subhalo at  $z = 0$  (subhalo 392276 at snapshot 99). We refer to this subhalo as our subhalo of interest (SoI).

### 2.2. *Bar Catalog*

In order to study the evolution of the morphology of our SoI, we make use of the Zana et al. (2022) catalog. They provide a decomposition of all galaxies with at least  $10^4$  star particles, as well as an estimate of the bar strength. This taken to be the maximum of the second Fourier mode ( $A_{2,\text{max}}$ ) within the bar region (not including spiral arms).

### 2.3. *Observations*

We make use of two observational data sets. First, we use the ASPCAP DR17 catalog of stellar abundances (García Pérez et al. 2016, J.A. Holtzman et al., in preparation). We make the same selection cuts as in Beane (2024), described in their Section 2.4. These are meant to select only giants with high quality abundance measurements as well as restricting the sample to only stars in the disk with angular momenta

similar to the Sun's. This results in a sample of 54,777 stars. We use Fe to track total metallicity and Mg alone as an  $\alpha$ -element.

We then further considered a dataset of stellar ages from the APOKASC2 catalog (Pinsonneault et al. 2018). This uses a combination of APOGEE spectroscopic parameters and *Kepler* time series photometry to compute astroseismic ages. Using only stars with 25% age uncertainties (taken as the maximum of the upper and lower uncertainty), we cross-match this catalog to our larger sample from ASPCAP which results in a sample of 1201 stars.

#### 2.4. One-Zone Chemical Evolution Model

James inserts his section

### 3. RESULTS

#### 3.1. Abundance Plane

The main result of our paper is given in Figure 1. Here, we compare the abundance plane in the Milky Way (left column) to that in our subhalo of interest (middle and right columns). The upper panels show the 2D distribution in the space of [Mg/Fe]-[Fe/H]. We have applied the standard `scipy` implementation of a gaussian kernel density estimator to a Cartesian grid of points. For each panel, we normalize so that the integral of the distribution is unity. Colors are plotted in a log scale ranging from 0.08 to 15 dex<sup>-2</sup>. Contour lines are plotted at 0.1, 1.5, and 10 dex<sup>-2</sup>.

The colored vertical lines are indicated at [Fe/H] = -0.75, -0.5, -0.25, and 0 dex in the Milky Way, and at bins 0.25 dex higher in the simulations. The lower panels show 1D histograms of [Mg/Fe] in bins centered on these values. The bins for the Milky Way/simulations have width 0.2/0.05 dex. The [Mg/Fe] values are given offsets so their medians are at zero. The rationale for the higher plotted [Fe/H] in the simulations comes just from the empirical location of the bimodalities. The Milky Way shows a clear bimodal population, with a high- $\alpha$  sequence most clearly distinct from the low- $\alpha$  sequence at low metallicity. The two sequences merge around solar metallicity.

Our SoI, on the other hand, does not show a clearly bimodal structure in the fiducial simulation (middle column). There is some structure in the [Fe/H] = -0.75 bin. The right panel of Figure 1 shows the same distribution as in the middle panel, but with a post-processed declination in [Mg/Fe] described in Section 2.1. Star particles formed before  $z = 1.5$  are given an additive offset of  $0.1 \times (t_{1.5} - t_{\text{form}})$ , where  $t_{1.5}$  is the age of the universe at  $z = 1.5$  and  $t_{\text{form}}$  is the formation time of the star particle. A multimodal structure emerges with three clear modes at [Mg/Fe]  $\sim 0.8, 0.5$ , and  $0.2$  dex. The 1D histograms show that the modes are well-separated, and that the troughs between the modes nearly vanish.

#### 3.2. Alpha Time Dependence

The abundance distributions shown in Figure 1 can be better understood by examining the evolution of [Mg/Fe] with time of the individual stars/star particles. In the upper panels of Figure 2 we show the true distribution of [Mg/Fe] as a function of time for the fiducial SoI in the middle and for the post-processed,  $\alpha$ -enhanced subhalo to the right. We use age instead of formation time in order to better facilitate comparisons to observations. These panels are true 2D histograms, with a logarithmic colormap normalized to the maximum of the plot. The values of [Mg/Fe] are offset so their medians are at zero.

There is a gap in the ages that occurs at an age of 10.6 Gyr, which we mark with a vertical dashed line. Star particles older than this line have a much clearer gradient in time with [Mg/Fe] than stars that form after. In the [Fe/H] = -0.25 bin, star particles which form directly after this line have a slightly depressed [Mg/Fe] than stars which form a short time later.

In the lower panels we plot to the left data from the Milky Way and to the middle and right from the fiducial and  $\alpha$ -enhanced SoI, respectively. For the simulations, we add 15% age and 0.01 dex [Mg/Fe] Gaussian errors. These values are roughly in line with the observational errors from the APOKASC2 and APOGEE datasets that the lower left panel is made from (see Appendix A for plots of the observational errors). The error in [Mg/Fe] is not significant, but the age error, which is 1.5 Gyr at 10 Gyr, smears out the distribution before and after the dashed line. The  $\alpha$ -enhanced SoI still shows two separate populations in this plot, but they now significantly overlap in age.

The Milky Way distribution (lower left panel) bears some resemblance to the  $\alpha$ -enhanced SoI. In particular, the [Fe/H] = -0.5 and -0.25 bins (blue and orange, respectively) show what appears to be two populations overlapping in age but nonetheless separated in [Mg/Fe]. These are the bins at which the bimodality is strongest (upper left panel of Figure 1).

#### 3.3. Evolutionary History

In an effort towards understanding the events in our SoI's history that led to the behavior around the dashed line in Figure 2, we examine the evolution of some of its key quantities. In the upper panel of Figure 3, we show the SFH of our galaxy with the same dashed line as in Figure 2 (at an age of 10.6 Gyr in that plot is at a time of  $\sim 3.2$  Gyr here). This SFH is computed using the SFR within twice the stellar half-mass radius in our SoI's main progenitors. We see two peaks in the SFH at  $t \sim 2.5$  and  $\sim 4.5$  Gyr of an amplitude of about 50 and  $30 M_\odot/\text{yr}$ . The dashed line corresponds to a relative drop in the SFR, down to about  $3 M_\odot/\text{yr}$  before quickly recovering.

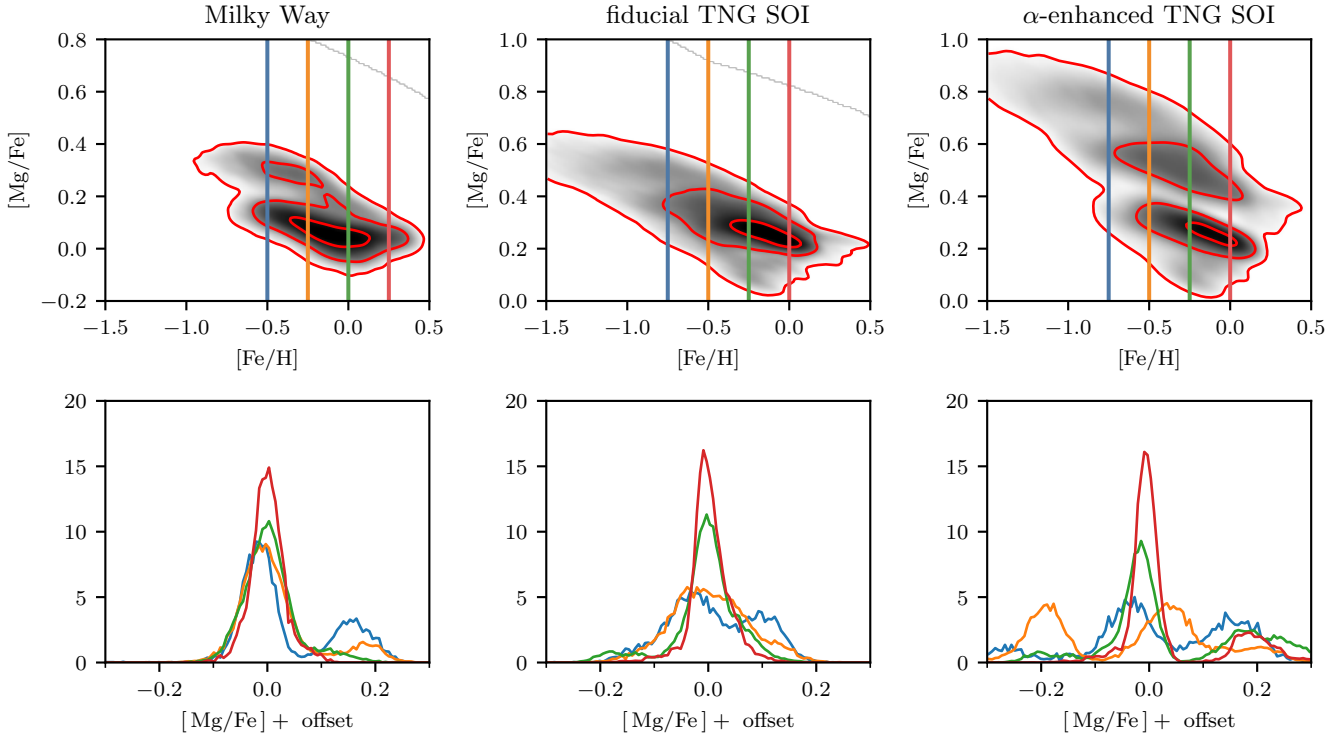


**Figure 1. When old stars are  $\alpha$ -enhanced, our subhalo of interest from TNG displays a prominent bimodality.** The upper left panel shows the distribution in the  $[\text{Mg}/\text{Fe}]$ - $[\text{Fe}/\text{H}]$  plane of the Milky Way, demonstrating a clear bimodality (data selection given in text). The lower left panel shows the 1D histograms of  $[\text{Mg}/\text{Fe}]$  at fixed  $[\text{Fe}/\text{H}]$  values of  $-0.5$ ,  $-0.25$ ,  $0$ , and  $0.25$  (blue, orange, green, and red, respectively). In the Milky Way, the bimodality is strongest at low metallicities while disappearing at high metallicities. The middle column shows the same plots but for our TNG subhalo of interest (392276) and with the fixed  $[\text{Fe}/\text{H}]$  values  $0.25$  dex lower. Only faint structure is seen in the lowest bin (blue,  $-0.75$  dex). The right column shows the same subhalo but after increasing the  $[\text{Mg}/\text{Fe}]$  value of star particles formed before  $z = 1.5$  linearly with formation time (specifically by incrementing  $[\text{Mg}/\text{Fe}]$  by  $0.1 \times (t_{1.5} - t_{\text{form}})$  if  $t_{\text{form}} < t_{1.5}$ , where  $t_{1.5}$  is the age of the universe at  $z = 1.5$ ). A clear bimodality is shown in these panels which, unlike in the Milky Way, is present at all metallicities.

The middle panel shows the accretion rate of the central black hole as a fraction of the maximum (Eddington) accretion rate. Early in its history ( $t < 2$  Gyr), the subhalo experiences high accretion rates. The accretion rate then steadily declines until  $t \sim 5$  Gyr at which point it fails to show on this linear plot. However, at the dashed line ( $\sim 3.2$  Gyr) there is a localized peak in the accretion rate, maxing out at about 30% Eddington. This places the BH firmly in the thermal quasar mode, and allows it to inject large amounts of thermal energy into the center of the galaxy.

The lower panel shows the virial mass of the subhalo, as measured by  $M_{200}$  – the mass within the radius that encloses a region of density  $200\times$  the mean density of the universe. Early on at  $t < 4$  Gyr the virial mass grows roughly linearly up to  $\sim 2 \times 10^{12} M_\odot$ . After that, the virial mass remains roughly constant until sharp increases at  $t \sim 10$  and  $\sim 12$  Gyr. The transition in the virial mass from linear to constant at  $t \sim 4$  Gyr is followed 1 Gyr later by a sudden drop in the SFR and BH accretion rate.

#### 3.4. Sequence of Events

Figure 4 presents surface density projections of gas and stars at different stages of the high- to low- $\alpha$  transition. The upper panels show gas density, while the lower panels display stellar density. Time progresses from  $\sim 2.4$  to  $\sim 3.6$  Gyr, corresponding to redshifts ranging from  $z \sim 2.7$  to  $z \sim 1.8$ .

The sequence of events is as follows:

1. A steady increase in the bar strength, as indicated by  $A_2/A_0$  for star particles with  $R < 2$  kpc, from  $\sim$  starting around 2.8 Gyr. This rise is accompanied by a notable change in the gas and stellar distributions, particularly in the development of elongated features consistent with the formation of a bar.
2. **Black Hole Accretion Spike:** Following the increase in bar strength, the black hole accretion rate (plotted as  $\dot{M}_{\text{BH}}/\dot{M}_{\text{Edd}}$ ) shows a significant spike. This occurs shortly after the peak in bar strength, suggesting a temporal correlation between bar development and enhanced gas inflow into the central region.
3. **Star Formation Rate Decline:** After the increase in black hole accretion, the star formation rate (SFR) be-

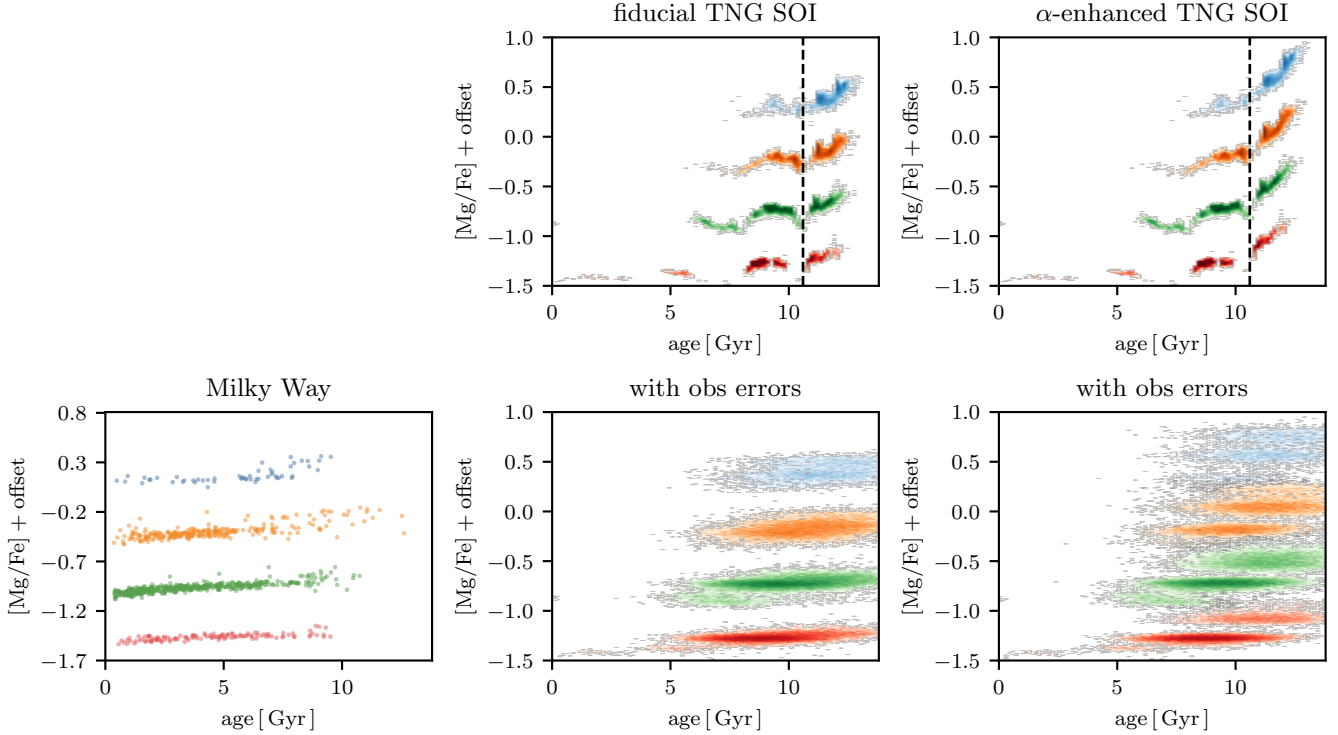


**Figure 2. Bimodality in the abundance plane is linked to distinct epochs in simulation.** The upper panels show  $[\text{Mg}/\text{Fe}]$  as a function of age for our subhalo in TNG. The colors indicate stellar populations at fixed values of  $[\text{Fe}/\text{H}]$ , which are the same as in Figure 1. A gap in the relation occurs at an age of approximately 10.6 Gyr, which we indicate with a vertical dashed line. The effect of the  $\alpha$ -enhancement is clear, as it separates the stars that form before and after this gap in ages (star particles which formed before  $z = 1.5$  are  $\alpha$ -enhanced, which occurs at an age of  $\sim 9.5$  Gyr). The lower panels show on the left the Milky Way and on the center and right the data from TNG but with 15% age errors and 0.01 dex errors in  $[\text{Mg}/\text{Fe}]$ . When the simulations are given these errors, we see that the before and after star particles smear such that the two populations significantly overlap in ages. In the  $\alpha$ -enhanced SoI, two populations emerge in each bin which overlapped in the fiducial distribution. This feature more closely resembles the Milky Way, which displays such populations where the bimodality is strongest –  $[\text{Fe}/\text{H}] = -0.5$  (blue) and  $-0.25$  (orange).

gins to decline. The decrease in SFR is gradual and continues as the black hole accretion rate remains elevated. By approximately 3.2 Gyr, the SFR reaches a more quiescent state, where it remains relatively low.

These projections and time series data highlight the sequential nature of bar formation, black hole accretion, and the subsequent suppression of star formation activity.

### 3.5. One-Zone Model

We showed in Figure 1 that a time-linear  $\alpha$ -enhancement of old stars (forming before  $z = 1.5$ ) led to the emergence of a strong chemical bimodality. This  $\alpha$ -enhancement is equivalent to saying that  $[\alpha/\text{Fe}]$  declines more rapidly with time at high- $z$ . In Figure 5 we demonstrate an argument for why this steeper decline in  $[\alpha/\text{Fe}]$  might be absent in TNG.

We show in the upper panel the evolution of  $[\text{Mg}/\text{Fe}]$  of three one zone chemical evolution models which vary the star formation (SF) timescale. This timescale,  $\tau_\star$ , is the inverse of the SF efficiency. A shorter SF timescale leads to a more rapid reduction in  $[\text{Mg}/\text{Fe}]$ . In the shortest timescale model,  $\tau_\star =$

0.5 Gyr,  $[\text{Mg}/\text{Fe}]$  drops from  $\sim 0.45$  to 0.08 dex in 2 Gyr. In comparison, the longest timescale model,  $\tau_\star = 5$  Gyr only drops to  $\sim 0.2$  dex in the same time.

The lower panel shows the negative of the time derivative of  $[\text{Mg}/\text{Fe}]$ . This panel shows the same behavior, with the slope of the  $\tau_\star = 0.5$  Gyr model peaking at  $-0.5$  dex/Gyr compared to the 5 Gyr model which peaks at  $-0.25$  dex/Gyr. After 1 Gyr, the trend starts to reverse, with the longer SF timescale models declining more rapidly, though at a much reduced rate ( $\sim -0.1$  dex/Gyr) than at the peak.

## 4. DISCUSSION

In Figure 1, we compared the abundance plane between the Milky Way and our SoI before and after the  $\alpha$ -enhancement. It is visibly obvious that the TNG SoI is unimodal before the  $\alpha$ -enhancement and bimodal afterwards (ignoring the minor mode at high- $[\text{Mg}/\text{Fe}]$ ). Here, we briefly discuss two main points: (1) assuming the  $\alpha$ -enhancement is justified, what leads to the bimodality in the SoI?, and (2) what justifies the

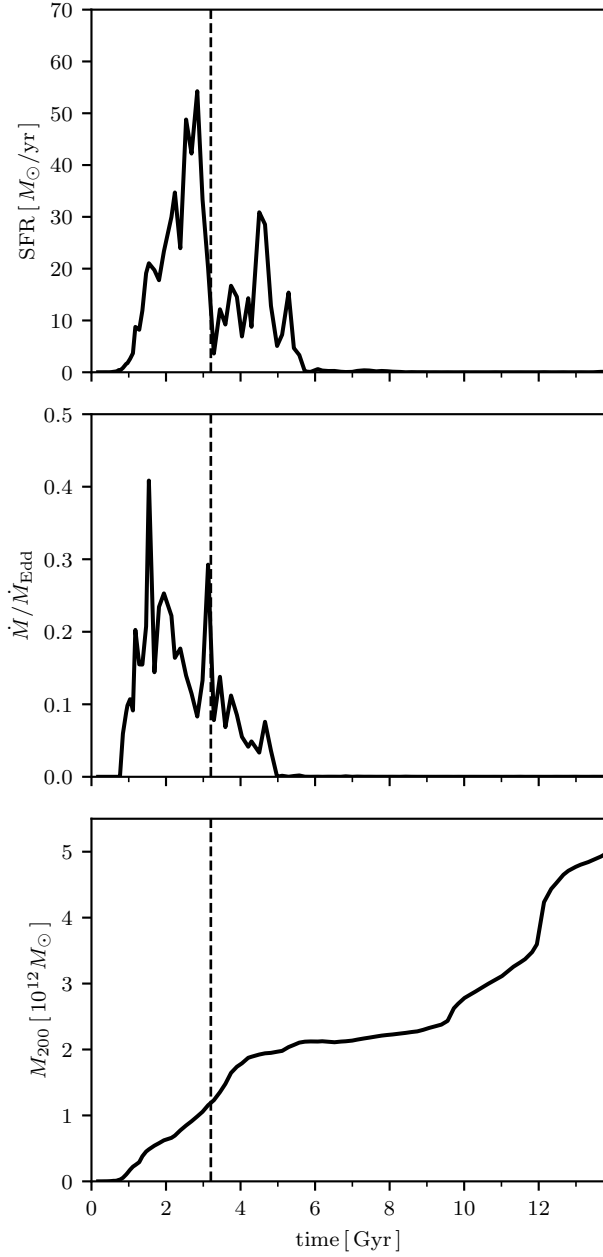


**Figure 3. The evolutionary history of our subhalo of interest.** The upper panel shows the SFH of our subhalo. This SFH is computed using the SFR within twice the stellar half-mass radius in our SoI’s main progenitors. In this and all subsequent panels we show a vertical dashed line at the same position as in Figure 2 ( $\sim 3.2$  Gyr), which delineates the separation between the high- and low- $\alpha$  sequences. The gap in ages is naturally associated with a gap in the SFH located at the dashed line. The middle panel shows the BH accretion rate as a fraction of the maximum (Eddington) accretion rate across time. The accretion rate is high early on, but then drops. The gap in ages (dashed line) is coincident with a local peak in the BH accretion rate. In the lower panel we show the mass assembly of the halo, given as the mass within the radius that encloses  $200\times$  the mean density of the universe. In this plot mergers are shown as sudden increases in  $M_{200}$ . Mergers at very early times when the halo is significantly less massive than its  $z=0$  mass are not shown, but one can see that no clear merger is associated with the gap in stellar ages. Two mergers occur later on at  $t \sim 10$  and  $\sim 12$  Gyr.

$\alpha$ -enhancement? We then briefly extend our comparison to the Milky Way data.

#### 4.1. Cause of Bimodality

An extensive analysis of our SoI is beyond the scope of this project, but here we argue that the evidence is consistent with the scenario presented in Beane (2024). They presented an idealized simulation resembling the merger between the Milky Way and GSE. They varied the orbital parameters slightly in a grid of 27 simulations and found that simulations which had a brief quiescent period as a result of the merger led to a bimodal abundance distribution. They argued that AGN activity was responsible for this brief quenching.

Once the  $\alpha$ -enhancement post-processing has been done, the SoI that we have studied in this work is consistent with this scenario. The vertical dashed line in Figures 2 and 3 denotes the transition between the high- and low- $\alpha$  sequences. We place it at an age of 10.6 Gyr or a formation time of  $\sim 3.2$  Gyr. The upper right panel of Figure 2 shows 2D histograms of [Mg/Fe] vs star particle age in fixed bins of [Fe/H] (each color is a different [Fe/H] bin, and an offset is given to [Mg/Fe] so their medians are at zero). Stars which formed before the dashed line had a steep decline of [Mg/Fe] with time, while the relation in star particles formed after the dashed line is much more flat. At the line, we see a gap in the [Fe/H] =  $-0.5$  and  $-0.25$  bins.

The age gap in each [Fe/H] bin of Figure 2 is contemporaneous with a minimum in the global SFR. We can see in the upper panel of Figure 3 that this dashed line lies almost exactly at the point of a local minimum in the SFH. This minimum, which is  $\sim 3 M_\odot/\text{yr}$ , is  $10\text{--}15\times$  smaller than the maxima before and after it.

During this period of suppressed SF, we argue that the relative lack of enrichment of Type II SNe which leads to a lower rate of Mg production. This leads to a rapid reduction in [Mg/Fe]. This, combined with a lack of SF in the first place, leads to a scarcity of star particles in the region intermediate between the high- and low- $\alpha$  sequences. A more in-depth explanation is given in Section 4.1 in Beane (2024).

In the fiducial TNG distribution shown in the upper middle panel of Figure 2, the same general behavior with respect to the dashed line is present. However, because the [Mg/Fe] decline before the dashed line is not as strong, star particles which formed before and after the dashed line overlap in the [Mg/Fe] distribution shown in Figure 1.

It is also worth noting that in both the fiducial and  $\alpha$ -enhanced SoI, there is a sort of rebound effect in [Mg/Fe]. The star particles which form directly after the dashed line have a slightly lower [Mg/Fe] than stars which form after. This was seen in Figure 9 of Beane (2024). In that work, it was argued that this occurs because, during the period of sup-

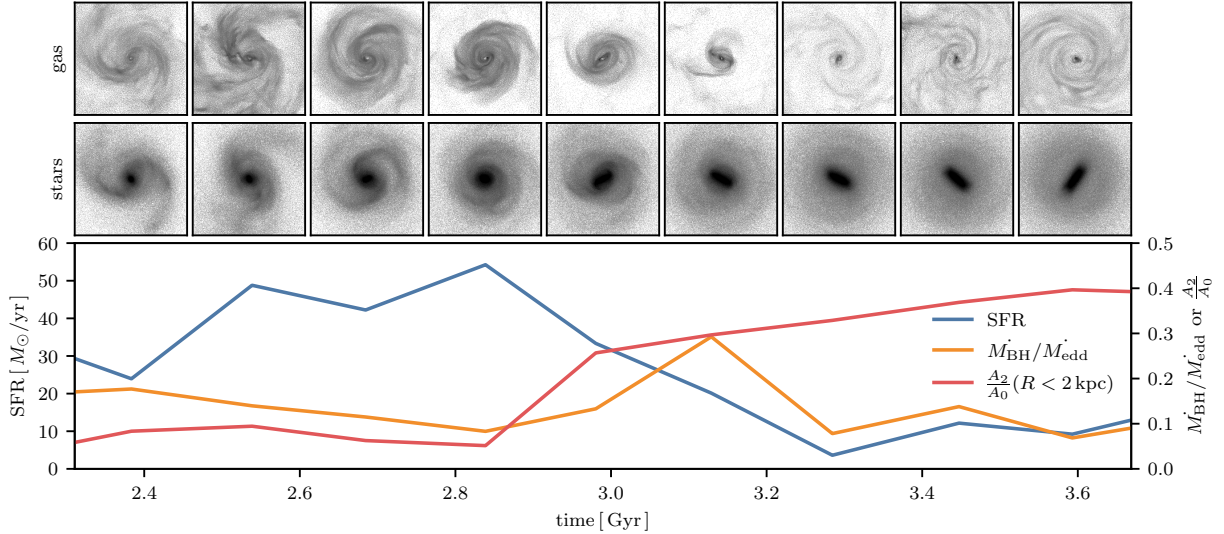


**Figure 4.** Surface density projections of gas (top row) and star particles (middle row) in our SoI across snapshots at different times during the high- to low- $\alpha$  transition. Below the projections is a plot showing the SFR, BH accretion rate (in units of  $\dot{M}_{\text{BH}}/\dot{M}_{\text{edd}}$ ), and bar strength ( $A_2/A_0$  for  $R < 2 \text{ kpc}$ ). Time ranges from  $\sim 2.4 \text{ Gyr}$  to  $\sim 3.6 \text{ Gyr}$ , corresponding to redshifts from  $z \sim 2.7$  to  $z \sim 1.8$ .

pressed SF, the  $[\alpha/\text{Fe}]$  of star forming gas plummets since there is no contribution from Type II SNe. Later, the  $[\alpha/\text{Fe}]$  of the gas will recover when the SFR also recovers, but there is a brief window when old, low- $\alpha$  stars can form.

#### 4.2. Steepening of $\alpha$ Decline

As described in Section 2.1, we applied a post-processing to the  $[\text{Mg}/\text{Fe}]$  of star particles in the TNG simulation. Specifically, for star particles formed before  $z = 1.5$ , we added to their  $[\text{Mg}/\text{Fe}]$  a value of  $0.1 \times (t_{1.5} - t_{\text{form}})$ , where  $t_{1.5}$  is the age of the universe at  $z = 1.5$  ( $\sim 4.3 \text{ Gyr}$ ) and  $t_{\text{form}}$  is the formation time. This post-processed subhalo is presented alongside the fiducial subhalo in the right and middle columns, respectively, of Figures 1 and 2.

The  $[\text{Mg}/\text{Fe}]$  value of star forming gas is the result of a complicated mixture of many different aspects of the TNG model, to name a few: stellar and AGN feedback which alter gas inflows and outflows, secular, dynamical evolution, SF prescription, magnetic fields, (lack of) cosmic rays, diffusivity of hydrodynamics solver, and, of course, enrichment models. Isolating the cause of the “incorrect”<sup>1</sup>  $[\text{Mg}/\text{Fe}]$  vs time evolution at high- $z$  is not straightforward nor, in our opinion, even possible. However, we do offer one reasonable explanation – the SFE at high densities, more present at high- $z$ , is too low.

<sup>1</sup>Our case study of a single galaxy, selected in a non-reproducible manner, is hardly cause to firmly assert that the fiducial evolution in TNG50 is incorrect.

We demonstrate the impact of the SFE on the  $[\alpha/\text{Fe}]$  ratio using a simple one-zone chemical evolution model with the publicly available code VICE. The details of our setup is given in Section 2.4. We vary the SF timescale,  $\tau_{\star} = M_{\text{gas}}/\text{SFR}$ , and examine the impact on the  $[\text{Mg}/\text{Fe}]$  ratio as a function of time. We find that shorter SF timescales do lead to a more rapid reduction in  $[\text{Mg}/\text{Fe}]$ . The rate of decrease in  $[\text{Mg}/\text{Fe}]$ , at its maximum, varies from  $\sim -0.25 \text{ dex/Gyr}$  in the  $\tau_{\star} = 5 \text{ Gyr}$  model to  $\sim -0.5 \text{ dex/Gyr}$  in the  $\tau_{\star} = 0.5 \text{ Gyr}$  model. For our post-processing, assumed an additional decrease rate of  $0.1 \text{ dex/Gyr}$ . Such a difference is well within the range of  $[\text{Mg}/\text{Fe}]$  decrease seen in our different  $\tau_{\star}$  models.

S. Hassan et al. (in preparation) demonstrated that the pressure regulated feedback model of Ostriker & Kim (2022) predicts higher SFRs of patches of gaseous disks in TNG50 than the fiducial model by up to an order of magnitude. This is well within our needed factor of 2 in  $\tau_{\star}$ . Therefore, our argument that the  $[\text{Mg}/\text{Fe}]$  does not decline quickly enough at high- $z$  is reasonably justified. An intuitive understanding of the impact the decline in  $[\alpha/\text{Fe}]$  vs time has is that, when  $[\alpha/\text{Fe}]$  declines rapidly, it is a better estimator of age. When it is a better estimator of age, events which are separated temporally become better separated in the abundance plane.

#### 4.3. Comparison to Observations

The lower left panel of Figure 2 shows the  $[\text{Mg}/\text{Fe}]$  vs age of stars in bins of  $[\text{Fe}/\text{H}]$  which pass our solar neighborhood selection and are present in the APOKASC2 catalog. In the bins where the bimodality is strongest (blue and orange,  $[\text{Fe}/\text{H}] = -0.5$  and  $-0.25$ , respectively), we see that there is a sort of two tiered distribution with significant overlap in

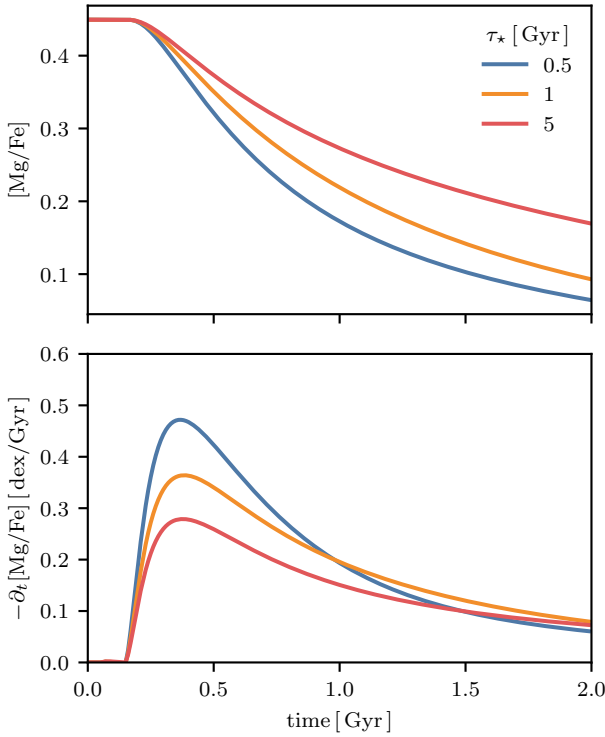


**Figure 5. A higher star formation efficiency leads to a steeper decline in [Mg/Fe].** In both panels, the lines show the time evolution of [Mg/Fe] in a simple one zone chemical evolution model, described in Section 2.4. The upper panel shows the evolution of [Mg/Fe] over 2 Gyr while the lower panel shows the negative of its time derivative. Decreasing the star formation timescale  $\tau_\star = M_{\text{gas}}/\text{SFR}$  leads to a more rapid decline in [Mg/Fe]. At its steepest decline ( $t \sim 0.5$  Gyr), an order of magnitude decrease in  $\tau_\star$  leads to a slope nearly a factor of 2 larger. At later times ( $t > 1$  Gyr), the models with smaller  $\tau_\star$  reach their steady-state [Mg/Fe] value more quickly.

age. In the SoI with age and abundance errors shown in the lower right panel, a very similar distribution can be seen in all [Fe/H] bins. An examination of the true distribution in the SoI (upper right panel), we see that the two distributions are in fact very cleanly separated in age. We do not know the true underlying distribution in the Milky Way, but these panels show that the general picture shown in our SoI is consistent with the Milky Way.

#### 4.4. Cause of Quiescence

It is natural to question why the minimum in the SFR occurs. In Beane (2024), AGN activity from a merger was the suspected cause. Here, we can see that there is indeed a brief burst in AGN accretion at the time of the merger (middle panel of Figure 3). Based on this burst, it is reasonable to suspect that AGN activity is also responsible for the quiescent period in our SoI. However, we argue that the cause of the localized

spike in the BH accretion rate is not due to a merger but instead due to the formation/strengthening of a bar.

In Figure ??, we take a closer view of the evolution of our SoI at the transition between the high- and low- $\alpha$  sequence, which we denote with the same line at an age of 10.6 Gyr ( $t \sim 3.2$  Gyr) as before. Here, we see that indeed the drop in the SFR ( $\sim 3.6 M_\odot/\text{yr}$  at  $t \sim 3.3$  Gyr) reaches a minimum one snapshot after the maximum in the BH accretion rate ( $\sim 0.3 \times M_{\text{edd}}$  at  $t \sim 3.1$  Gyr).

The gaseous surface density images in Figure ?? are helpful to understand this moment in the SoI’s history. The third row, from  $t = 2.84$  to 3.28 Gyr shows this moment, with the right-most  $t = 3.28$  Gyr marking the transition from high- to low- $\alpha$  formation. The gas fraction (bottom right number) quickly drops from 25% to 3%, accompanied by not only a high SFR ( $54.3 M_\odot/\text{yr}$  at maximum) but also an increasing BH accretion rate.

This increasing BH accretion rate is also preceded by the formation of a stellar bar at the center of the galaxy as seen in Figure ??.<sup>2</sup> Starting from  $t = 2.38$  Gyr, the bar strength grows from  $A_{2,\text{max}} = 0.1$  to 0.5 at  $t = 3.13$  Gyr, the peak of the BH accretion rate. Note that the bar strength considers only the region where the phase of the second Fourier mode is constant, and so spiral structure as seen in, e.g., the  $t = 2.38$  Gyr snapshot is not eligible for  $A_{2,\text{max}}$ .

The scenario implied by all the available evidence is that:

1. a bar forms through an internal instability, which
2. drives a large amount of gas to the center of the galaxy, which
3. triggers a high BH accretion rate and quasar-mode thermal feedback, which
4. clears gas out of the galaxy.

This picture is supported by work showing that in simulations bars should be able to fuel AGN (Shlosman et al. 1990; Hopkins & Quataert 2010), and that barred galaxies preferentially host AGN (Silva-Lima et al. 2022). At high- $z$ , the AGN mechanism is thought to be responsible for quenching (e.g. D’Eugenio et al. 2023; Park et al. 2024; Mićić et al. 2024; Belli et al. 2024, and references therein).

A complicating factor for this picture comes from the high SFR associated with the galaxy. The depletion time ( $M_{\text{gas}}/\text{SFR}$ ) at the  $t = 2.84$  Gyr snapshot is 204 Myr, shorter than the time it takes for the SFR to reach its minimum. However, this has to be balanced by the fact that the depletion time is already short at this redshift. The average depletion time in the preceding 5 snapshots is 220 Myr, so clearly the SoI

<sup>2</sup>The bar is already at a strength of  $A_{2,\text{max}} \sim 0.1$  before, so it either forms or strengthens depending on one’s interpretation. We choose the former.

is accreting high amounts of gas from its CGM. A definitive account, difficult with the current simulation because of its sparse snapshot spacing, requires further work.

## 5. CONCLUSIONS

In this work, we examined a specific subhalo in Illustris TNG50. This subhalo is at a Milky Way-progenitor mass at high- $z$  ( $z \sim 2$ ). After applying a post-processing step that increased the [Mg/Fe] of star particles formed before  $z = 1.5$ , this subhalo hosts a strong bimodality in the plane of [Mg/Fe] and [Fe/H], shown in Figure 1. This post-processing is justified by arguing that the SFE of dense gas is too low in TNG (Section 4.2).

This bimodality can be traced to an event that occurred at an age of 10.6 Gyr, or formation time of  $\sim 3.2$  Gyr ( $z \sim 2$ ). Shown as a vertical dashed line in Figure 2, star particles which form before this form at high- $\alpha$  while stars which form after form at lower  $\alpha$ . At the dashed line, there is a gap. We argue that the presence of this gap is responsible for the valley in the bimodality (Figure 1). It is accompanied by a global reduction in the SFR by about a factor of 6 (upper panel of Figure 3).

The reduction in the SFR has two effects. First, a lower production of Mg is the natural result of a lack of Type II SNe. Second, the lack of SF means that stars at [Mg/Fe] intermediate between the high- and low- $\alpha$  sequences never form. This is the same argument that was first presented in Beane (2024). When observational errors are added to the subhalo's abundance vs age distribution, we show that it is broadly consistent with the Milky Way's abundance-age distribution (Section 4.3).

While a strong claim about the cause of the quiescent period is difficult to make, we showed that the formation/strengthening of a bar could be responsible for triggering an episode of AGN activity. This work adds further support that the argument made in Beane (2024) is a plausible explanation for the Milky Way's abundance bimodality.

<sup>1</sup> This work has made use of data from the European Space Agency (ESA) mission *Gaia* (<https://www.cosmos.esa.int/gaia>), processed by the *Gaia* Data Processing and Analysis Consortium (DPAC, <https://www.cosmos.esa.int/web/gaia/dpac/consortium>). Funding for the DPAC has been provided by national institutions, in particular the institutions participating in the *Gaia* Multilateral Agreement.

## REFERENCES

- Adibekyan, V. Z., Santos, N. C., Sousa, S. G., & Israelian, G. 2011, *A&A*, 535, L11, doi: [10.1051/0004-6361/201118240](https://doi.org/10.1051/0004-6361/201118240)
- Adibekyan, V. Z., Sousa, S. G., Santos, N. C., et al. 2012, *A&A*, 545, A32, doi: [10.1051/0004-6361/201219401](https://doi.org/10.1051/0004-6361/201219401)
- Beane, A. 2024, arXiv e-prints, arXiv:2407.07985, doi: [10.48550/arXiv.2407.07985](https://doi.org/10.48550/arXiv.2407.07985)
- Belli, S., Park, M., Davies, R. L., et al. 2024, *Nature*, 630, 54, doi: [10.1038/s41586-024-07412-1](https://doi.org/10.1038/s41586-024-07412-1)
- Belokurov, V., Erkal, D., Evans, N. W., Koposov, S. E., & Deason, A. J. 2018, *MNRAS*, 478, 611, doi: [10.1093/mnras/sty982](https://doi.org/10.1093/mnras/sty982)
- Bensby, T., Feltzing, S., & Oey, M. S. 2014, *A&A*, 562, A71, doi: [10.1051/0004-6361/201322631](https://doi.org/10.1051/0004-6361/201322631)
- Bernaldo e Silva, L., Debattista, V. P., Khachaturyants, T., & Nidever, D. 2020, *MNRAS*, 492, 4716, doi: [10.1093/mnras/staa065](https://doi.org/10.1093/mnras/staa065)
- Bernaldo e Silva, L., Debattista, V. P., Nidever, D., Amarante, J. A. S., & Garver, B. 2021, *MNRAS*, 502, 260, doi: [10.1093/mnras/staa3966](https://doi.org/10.1093/mnras/staa3966)
- Bland-Hawthorn, J., & Gerhard, O. 2016, *ARA&A*, 54, 529, doi: [10.1146/annurev-astro-081915-023441](https://doi.org/10.1146/annurev-astro-081915-023441)
- Bondi, H. 1952, *MNRAS*, 112, 195, doi: [10.1093/mnras/112.2.195](https://doi.org/10.1093/mnras/112.2.195)
- Bondi, H., & Hoyle, F. 1944, *MNRAS*, 104, 273, doi: [10.1093/mnras/104.5.273](https://doi.org/10.1093/mnras/104.5.273)
- Brook, C., Richard, S., Kawata, D., Martel, H., & Gibson, B. K. 2007, *ApJ*, 658, 60, doi: [10.1086/511056](https://doi.org/10.1086/511056)
- Brook, C. B., Gibson, B. K., Martel, H., & Kawata, D. 2005, *ApJ*, 630, 298, doi: [10.1086/431924](https://doi.org/10.1086/431924)
- Brook, C. B., Kawata, D., Gibson, B. K., & Freeman, K. C. 2004, *ApJ*, 612, 894, doi: [10.1086/422709](https://doi.org/10.1086/422709)
- Buck, T. 2020, *MNRAS*, 491, 5435, doi: [10.1093/mnras/stz3289](https://doi.org/10.1093/mnras/stz3289)
- Chandra, V., Semenov, V. A., Rix, H.-W., et al. 2024, *ApJ*, 972, 112, doi: [10.3847/1538-4357/ad5b60](https://doi.org/10.3847/1538-4357/ad5b60)
- Chiappini, C. 2009, in *The Galaxy Disk in Cosmological Context*, ed. J. Andersen, Nordströara, B. m, & J. Bland-Hawthorn, Vol. 254, 191–196, doi: [10.1017/S1743921308027580](https://doi.org/10.1017/S1743921308027580)
- Chiappini, C., Matteucci, F., & Gratton, R. 1997, *ApJ*, 477, 765, doi: [10.1086/303726](https://doi.org/10.1086/303726)
- Ciucă, I., Kawata, D., Ting, Y.-S., et al. 2024, *MNRAS*, 528, L122, doi: [10.1093/mnrasl/slad033](https://doi.org/10.1093/mnrasl/slad033)
- Clarke, A. J., Debattista, V. P., Nidever, D. L., et al. 2019, *MNRAS*, 484, 3476, doi: [10.1093/mnras/stz104](https://doi.org/10.1093/mnras/stz104)
- D'Eugenio, F., Perez-Gonzalez, P., Maiolino, R., et al. 2023, arXiv e-prints, arXiv:2308.06317, doi: [10.48550/arXiv.2308.06317](https://doi.org/10.48550/arXiv.2308.06317)
- Fuhrmann, K. 1998, *A&A*, 338, 161

- . 2004, Astronomische Nachrichten, 325, 3, doi: [10.1002/asna.200310173](https://doi.org/10.1002/asna.200310173)
- García Pérez, A. E., Allende Prieto, C., Holtzman, J. A., et al. 2016, AJ, 151, 144, doi: [10.3847/0004-6256/151/6/144](https://doi.org/10.3847/0004-6256/151/6/144)
- Garver, B. R., Nidever, D. L., Debattista, V. P., Beraldo e Silva, L., & Khachaturyants, T. 2023, ApJ, 953, 128, doi: [10.3847/1538-4357/acdfc6](https://doi.org/10.3847/1538-4357/acdfc6)
- Gratton, R., Carretta, E., Matteucci, F., & Sneden, C. 1996, in Astronomical Society of the Pacific Conference Series, Vol. 92, Formation of the Galactic Halo...Inside and Out, ed. H. L. Morrison & A. Sarajedini, 307
- Grisoni, V., Spitoni, E., Matteucci, F., et al. 2017, MNRAS, 472, 3637, doi: [10.1093/mnras/stx2201](https://doi.org/10.1093/mnras/stx2201)
- Hayden, M. R., Bland-Hawthorn, J., Sharma, S., et al. 2020, MNRAS, 493, 2952, doi: [10.1093/mnras/staa335](https://doi.org/10.1093/mnras/staa335)
- Helmi, A., Babusiaux, C., Koppelman, H. H., et al. 2018, Nature, 563, 85, doi: [10.1038/s41586-018-0625-x](https://doi.org/10.1038/s41586-018-0625-x)
- Hopkins, P. F., & Quataert, E. 2010, MNRAS, 407, 1529, doi: [10.1111/j.1365-2966.2010.17064.x](https://doi.org/10.1111/j.1365-2966.2010.17064.x)
- Hoyle, F., & Lyttleton, R. A. 1939, Proceedings of the Cambridge Philosophical Society, 35, 405, doi: [10.1017/S0305004100021150](https://doi.org/10.1017/S0305004100021150)
- Khoperskov, S., Haywood, M., Snaith, O., et al. 2021, MNRAS, 501, 5176, doi: [10.1093/mnras/staa3996](https://doi.org/10.1093/mnras/staa3996)
- Mičić, M., Irwin, J. A., Nair, P., et al. 2024, arXiv e-prints, arXiv:2405.18685. <https://arxiv.org/abs/2405.18685>
- Naidu, R. P., Conroy, C., Bonaca, A., et al. 2020, ApJ, 901, 48, doi: [10.3847/1538-4357/abaef4](https://doi.org/10.3847/1538-4357/abaef4)
- Nelson, D., Pillepich, A., Springel, V., et al. 2019, MNRAS, 490, 3234, doi: [10.1093/mnras/stz2306](https://doi.org/10.1093/mnras/stz2306)
- Nidever, D. L., Bovy, J., Bird, J. C., et al. 2014, ApJ, 796, 38, doi: [10.1088/0004-637X/796/1/38](https://doi.org/10.1088/0004-637X/796/1/38)
- Ostriker, E. C., & Kim, C.-G. 2022, ApJ, 936, 137, doi: [10.3847/1538-4357/ac7de2](https://doi.org/10.3847/1538-4357/ac7de2)
- Pakmor, R., Springel, V., Bauer, A., et al. 2016, MNRAS, 455, 1134, doi: [10.1093/mnras/stv2380](https://doi.org/10.1093/mnras/stv2380)
- Park, M., Belli, S., Conroy, C., et al. 2024, arXiv e-prints, arXiv:2404.17945, doi: [10.48550/arXiv.2404.17945](https://doi.org/10.48550/arXiv.2404.17945)
- Pillepich, A., Springel, V., Nelson, D., et al. 2018, MNRAS, 473, 4077, doi: [10.1093/mnras/stx2656](https://doi.org/10.1093/mnras/stx2656)
- Pillepich, A., Nelson, D., Springel, V., et al. 2019, MNRAS, 490, 3196, doi: [10.1093/mnras/stz2338](https://doi.org/10.1093/mnras/stz2338)
- Pinsonneault, M. H., Elsworth, Y. P., Tayar, J., et al. 2018, ApJS, 239, 32, doi: [10.3847/1538-4365/aaebfd](https://doi.org/10.3847/1538-4365/aaebfd)
- Reddy, B. E., Lambert, D. L., & Allende Prieto, C. 2006, MNRAS, 367, 1329, doi: [10.1111/j.1365-2966.2006.10148.x](https://doi.org/10.1111/j.1365-2966.2006.10148.x)
- Richard, S., Brook, C. B., Martel, H., et al. 2010, MNRAS, 402, 1489, doi: [10.1111/j.1365-2966.2009.16008.x](https://doi.org/10.1111/j.1365-2966.2009.16008.x)
- Schönrich, R., & Binney, J. 2009, MNRAS, 396, 203, doi: [10.1111/j.1365-2966.2009.14750.x](https://doi.org/10.1111/j.1365-2966.2009.14750.x)
- Sharma, S., Hayden, M. R., & Bland-Hawthorn, J. 2021, MNRAS, 507, 5882, doi: [10.1093/mnras/stab2015](https://doi.org/10.1093/mnras/stab2015)
- Shlosman, I., Begelman, M. C., & Frank, J. 1990, Nature, 345, 679, doi: [10.1038/345679a0](https://doi.org/10.1038/345679a0)
- Silva-Lima, L. A., Martins, L. P., Coelho, P. R. T., & Gadotti, D. A. 2022, A&A, 661, A105, doi: [10.1051/0004-6361/202142432](https://doi.org/10.1051/0004-6361/202142432)
- Spitoni, E., Matteucci, F., Gratton, R., et al. 2024, arXiv e-prints, arXiv:2405.11025, doi: [10.48550/arXiv.2405.11025](https://doi.org/10.48550/arXiv.2405.11025)
- Spitoni, E., Silva Aguirre, V., Matteucci, F., Calura, F., & Grisoni, V. 2019, A&A, 623, A60, doi: [10.1051/0004-6361/201834188](https://doi.org/10.1051/0004-6361/201834188)
- Springel, V. 2010, MNRAS, 401, 791, doi: [10.1111/j.1365-2966.2009.15715.x](https://doi.org/10.1111/j.1365-2966.2009.15715.x)
- van Dokkum, P. G., Leja, J., Nelson, E. J., et al. 2013, ApJL, 771, L35, doi: [10.1088/2041-8205/771/2/L35](https://doi.org/10.1088/2041-8205/771/2/L35)
- Vogelsberger, M., Genel, S., Sijacki, D., et al. 2013, MNRAS, 436, 3031, doi: [10.1093/mnras/stt1789](https://doi.org/10.1093/mnras/stt1789)
- Weinberger, R., Springel, V., Hernquist, L., et al. 2017, MNRAS, 465, 3291, doi: [10.1093/mnras/stw2944](https://doi.org/10.1093/mnras/stw2944)
- Zana, T., Lupi, A., Bonetti, M., et al. 2022, MNRAS, 515, 1524, doi: [10.1093/mnras/stac1708](https://doi.org/10.1093/mnras/stac1708)

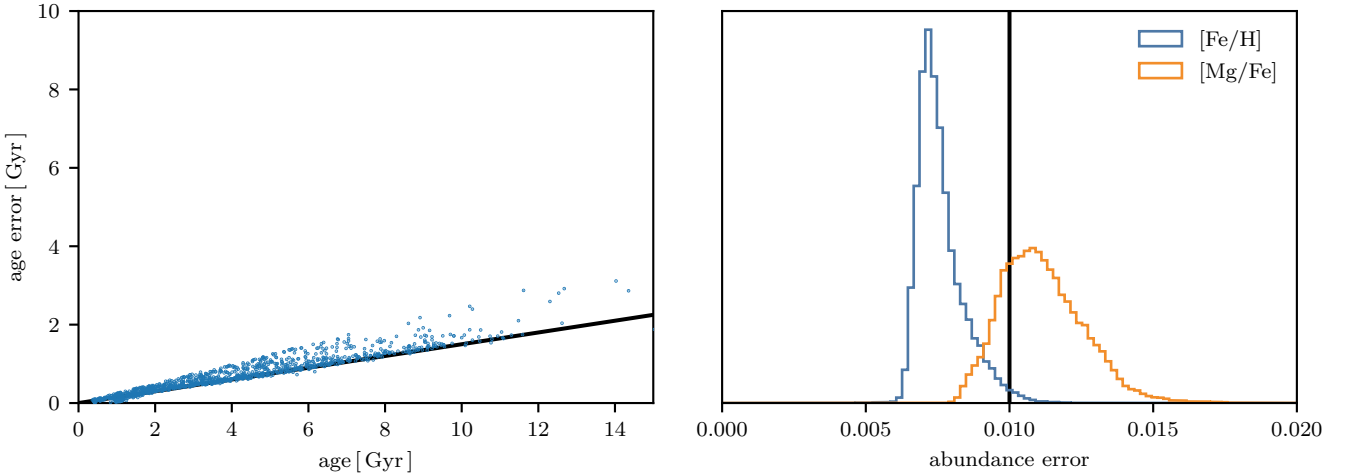


**Figure 6.** The observational errors of the APOKASC2 (left) and ASPCAP dataset (right). We show, on the left, a line indicating a 15% error in observed age and on the right a vertical line indicating a 0.01 dex error.

## APPENDIX

### A. OBSERVATIONAL ERRORS

In Figure 2, we assumed observational errors of 15% in age and 0.01 dex in [Mg/Fe]. In Figure 6, we plot the quoted observational errors of the APOKASC2 (left) and ASPCAP (right) datasets, showing both [Fe/H] and [Mg/Fe] (blue and orange, respectively). We show our 15% age error and 0.01 dex abundance error assumptions as black lines. For the age error, we used the maximum of the upper and lower estimates from Pinsonneault et al. (2018). Our assumed errors are generally consistent with the errors. Our error in [Mg/Fe] is a bit smaller than in ASPCAP, but the age estimates are by far the more constraining of the two.

### B. RANDOM SELECTION OF SUBHALOS

In Figures 7 to 23, we show a version of Figure 1 but for a random selection of subhalos from our broader sample of 168 Milky Way-progenitors at  $z = 1.5$  in TNG50. It is from this sample that we selected our SoI. We first show our SoI at  $z = 1.5$  in Figure 7, and then show our random sample of 16.

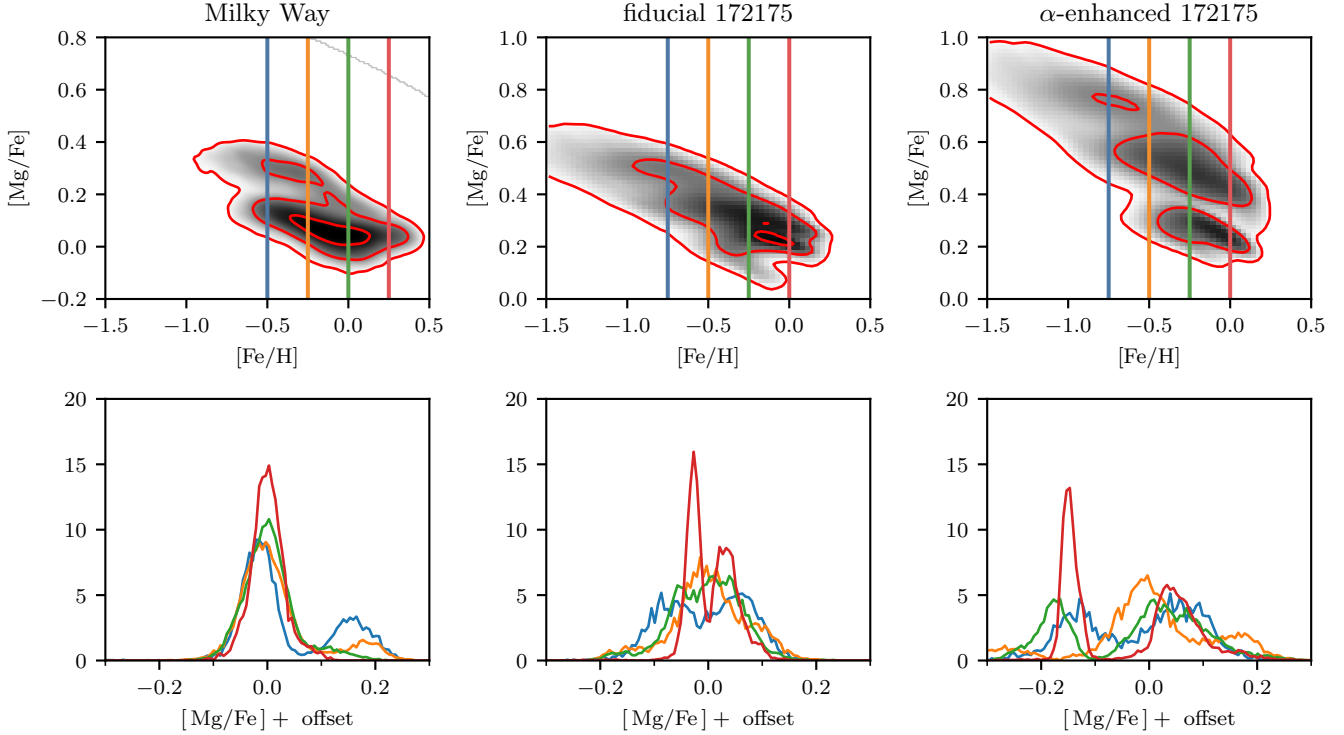


**Figure 7.** The same as Figure 1, but for our SoI at  $z = 1.5$ .

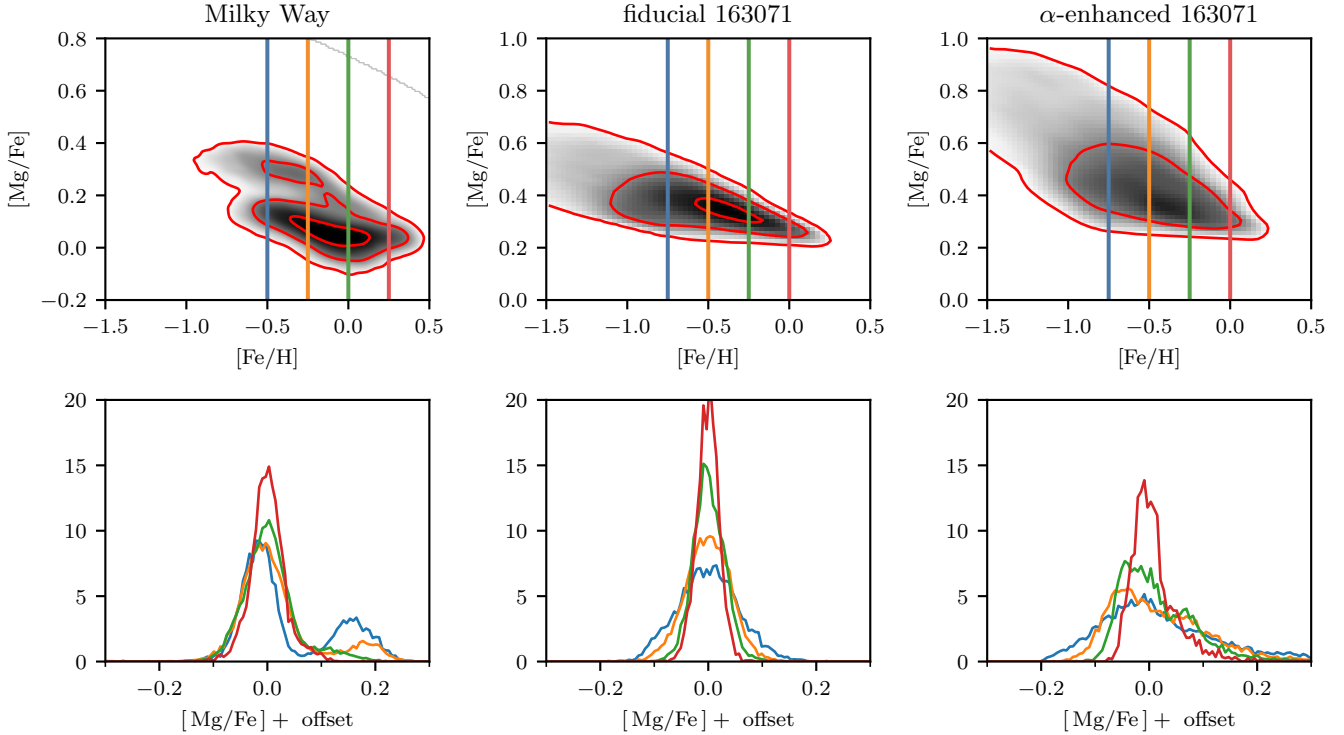


**Figure 8.** The same as Figure 1, but for a random subhalo from our catalog at  $z = 1.5$ .

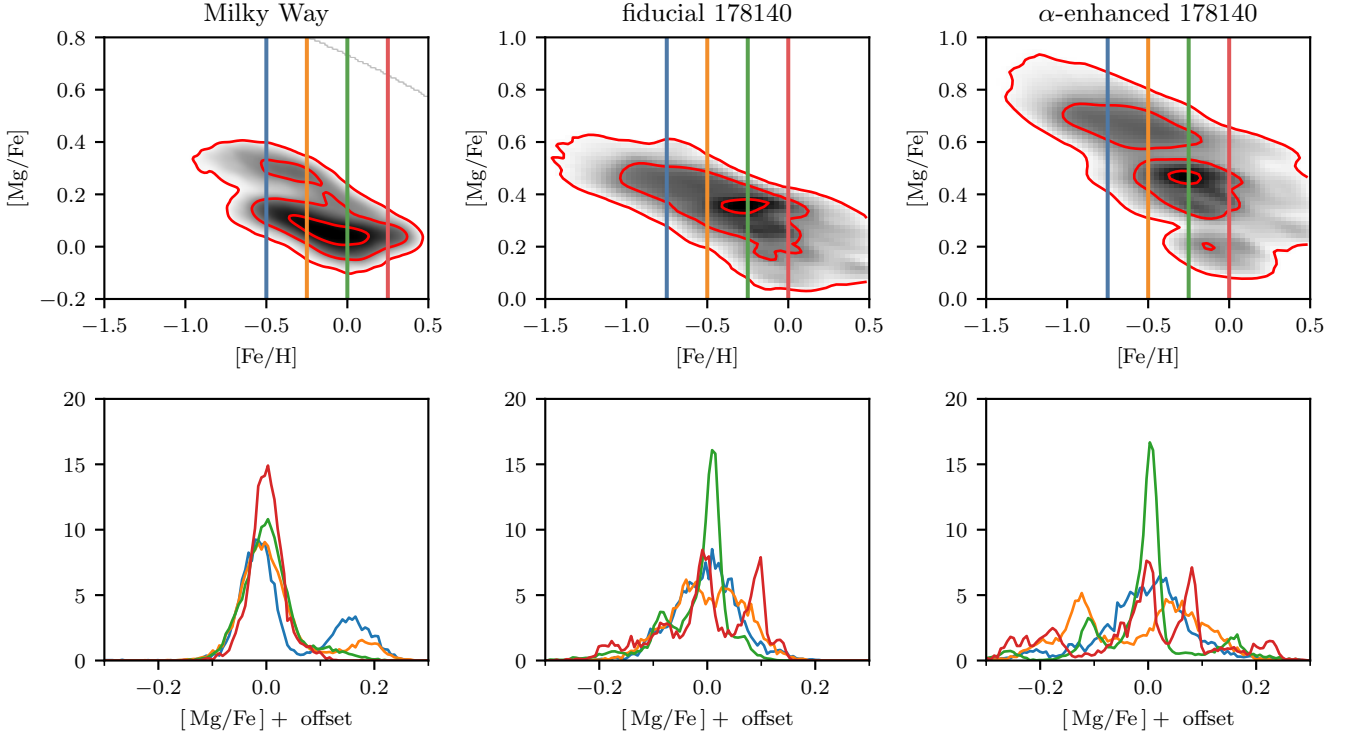


**Figure 9.** The same as Figure 1, but for a random subhalo from our catalog at  $z = 1.5$ .

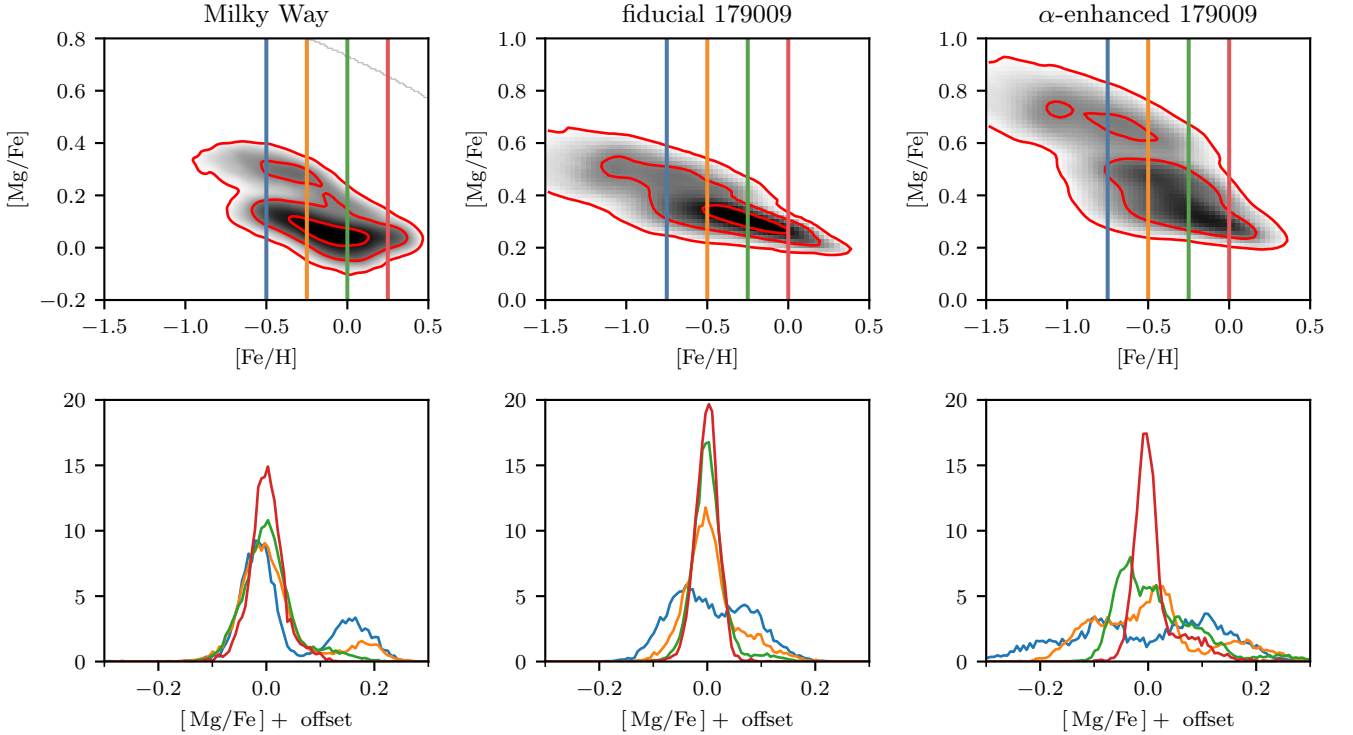


**Figure 10.** The same as Figure 1, but for a random subhalo from our catalog at  $z = 1.5$ .

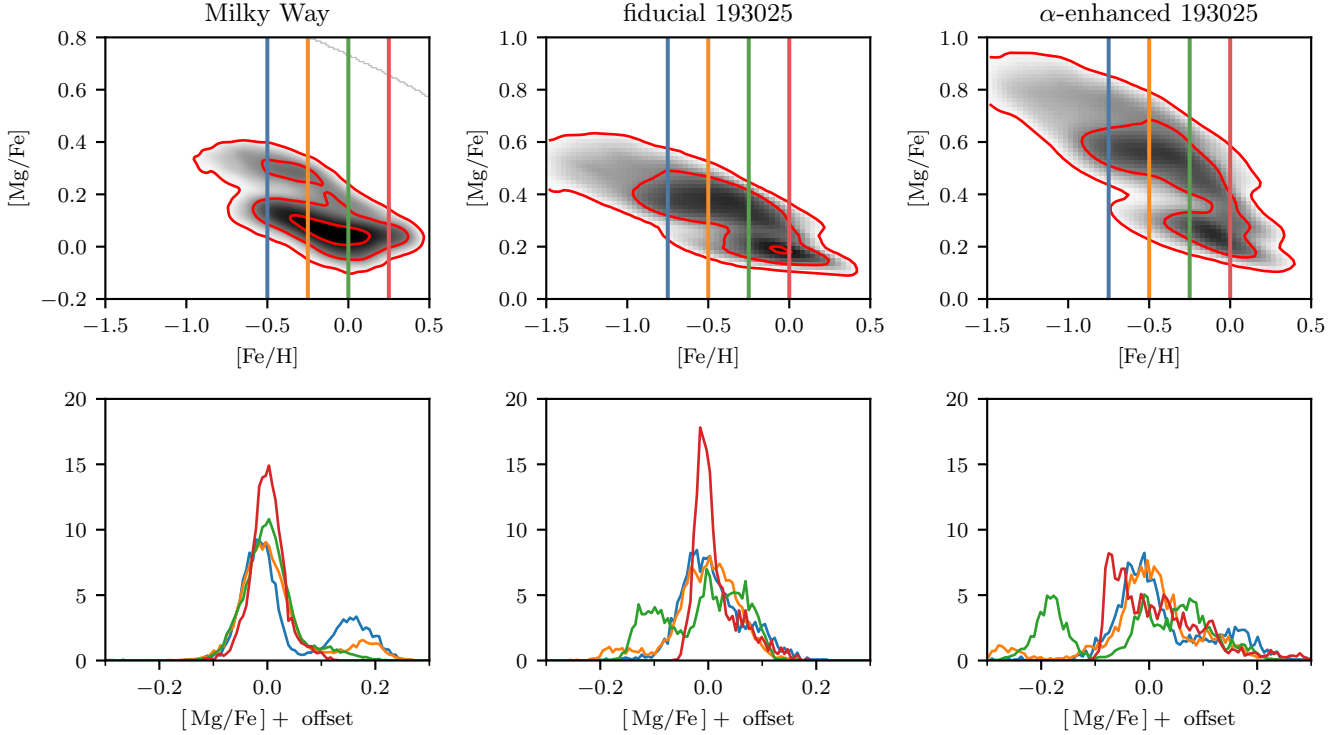


**Figure 11.** The same as Figure 1, but for a random subhalo from our catalog at  $z = 1.5$ .

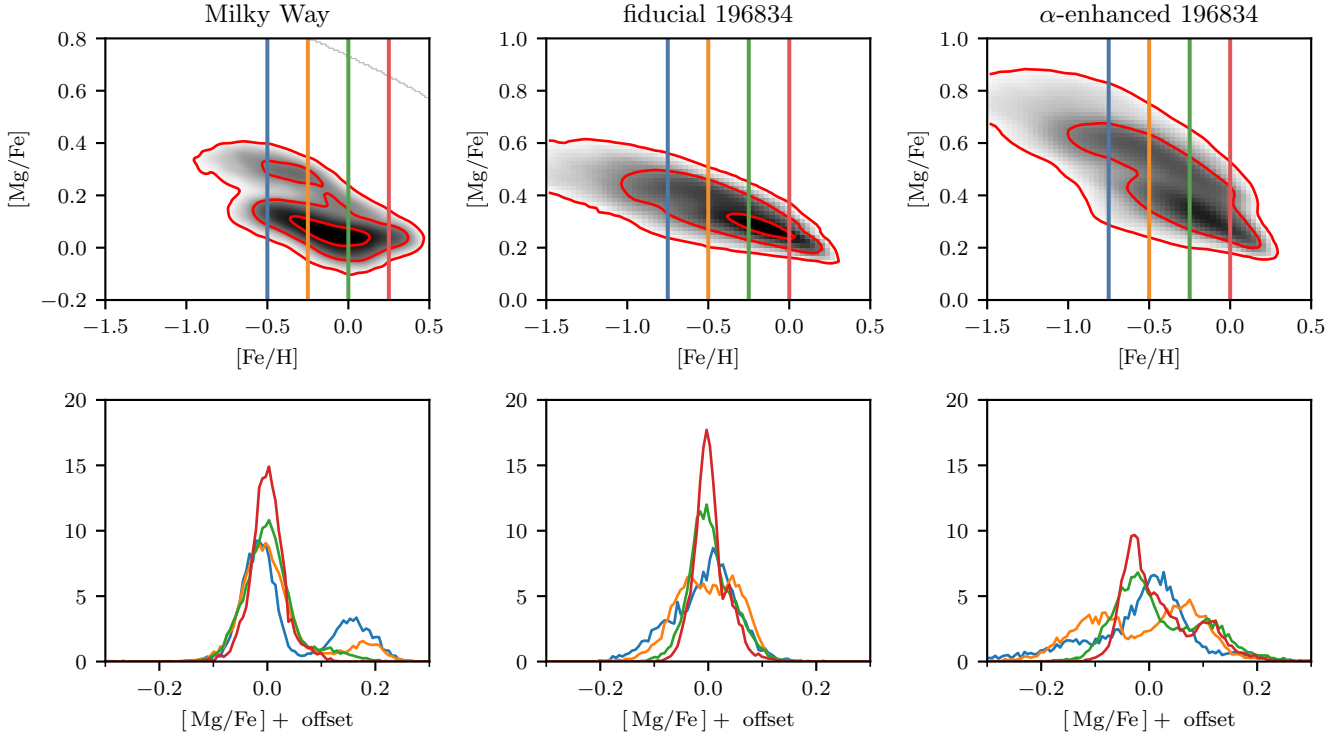


**Figure 12.** The same as Figure 1, but for a random subhalo from our catalog at  $z = 1.5$ .

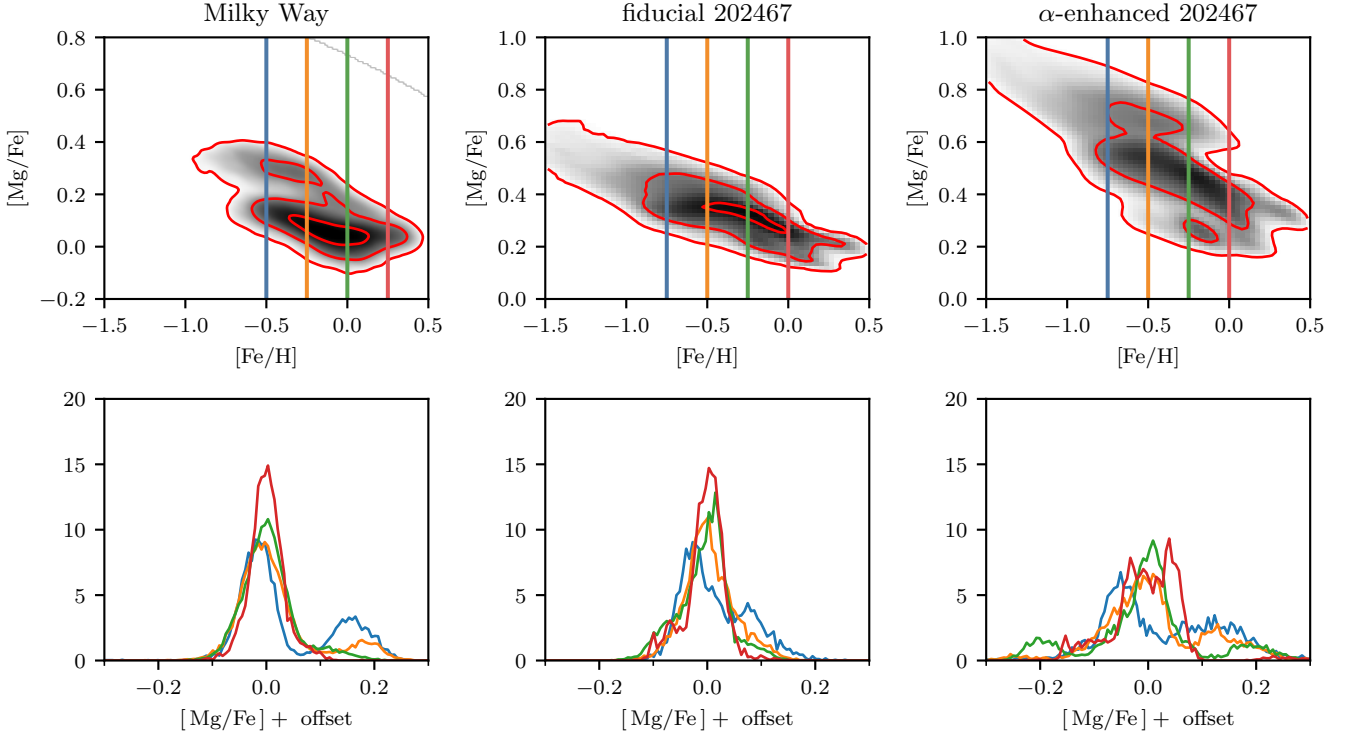


**Figure 13.** The same as Figure 1, but for a random subhalo from our catalog at  $z = 1.5$ .

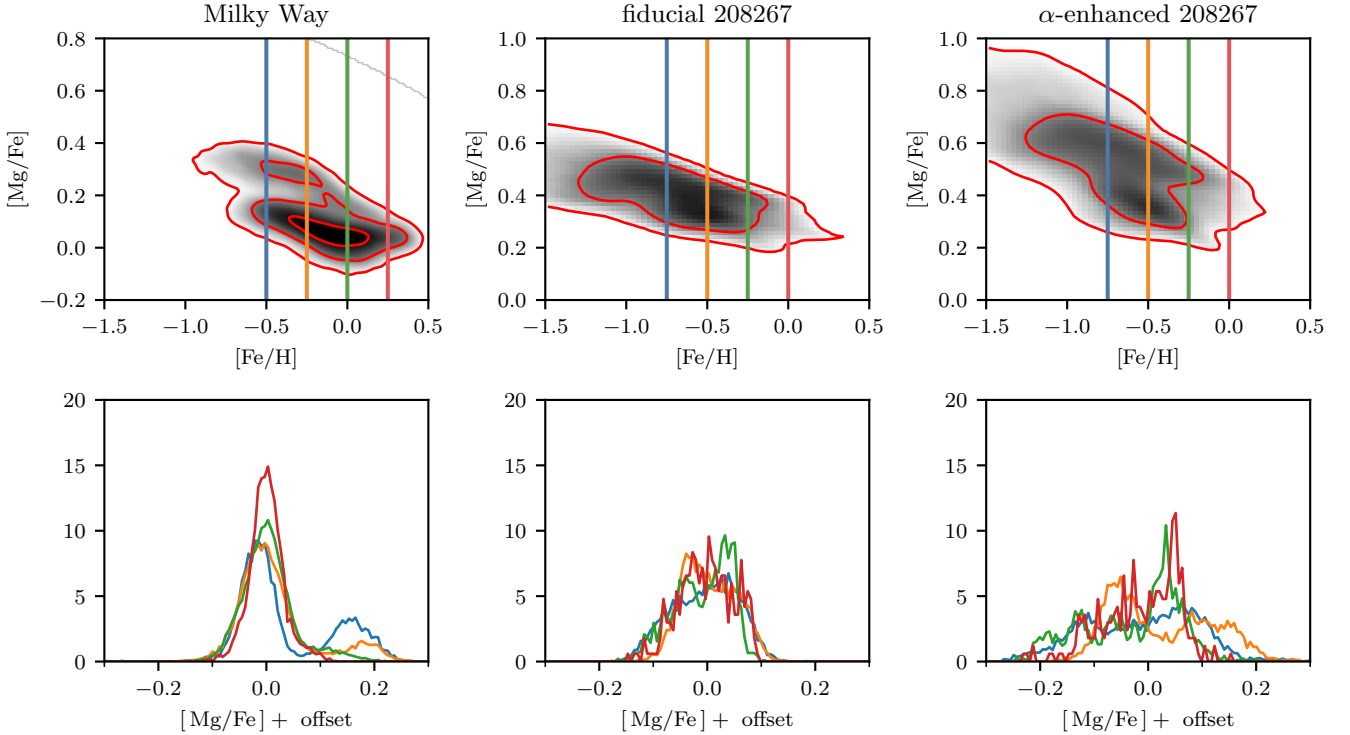


**Figure 14.** The same as Figure 1, but for a random subhalo from our catalog at  $z = 1.5$ .

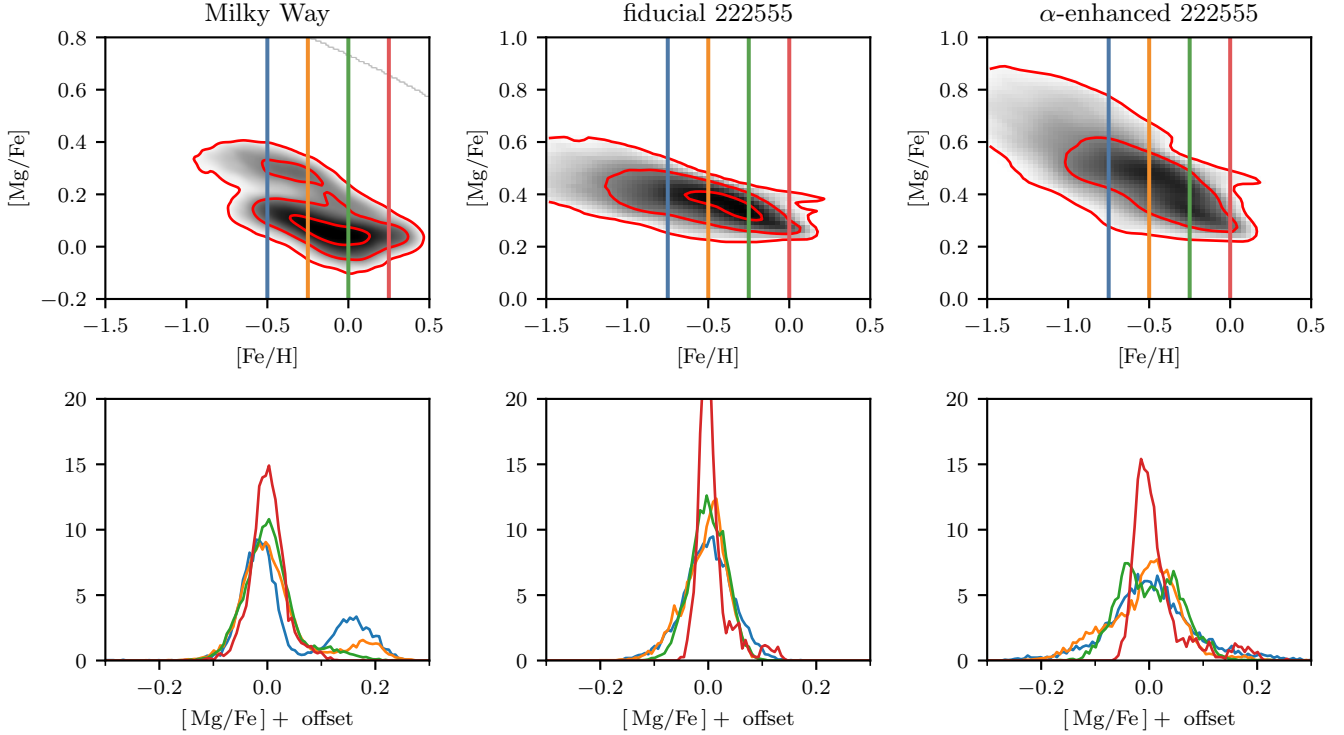


**Figure 15.** The same as Figure 1, but for a random subhalo from our catalog at  $z = 1.5$ .

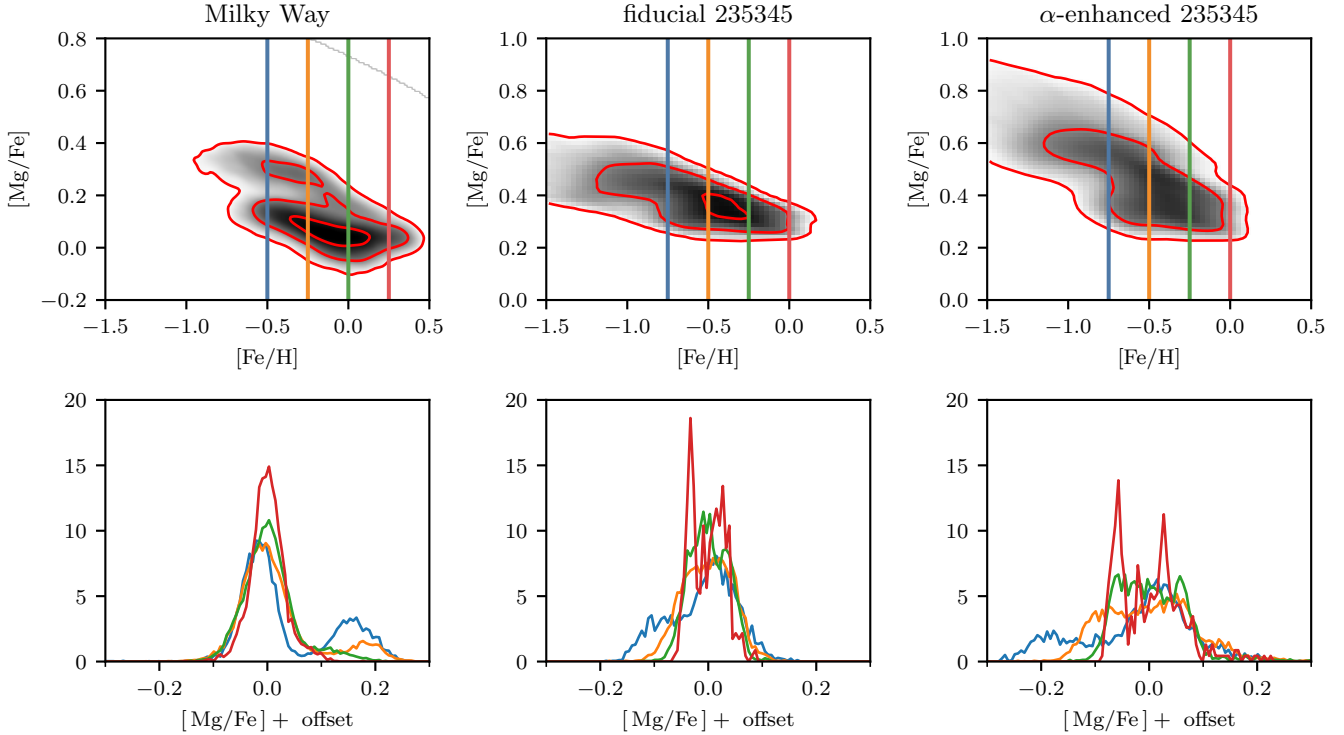


**Figure 16.** The same as Figure 1, but for a random subhalo from our catalog at  $z = 1.5$ .

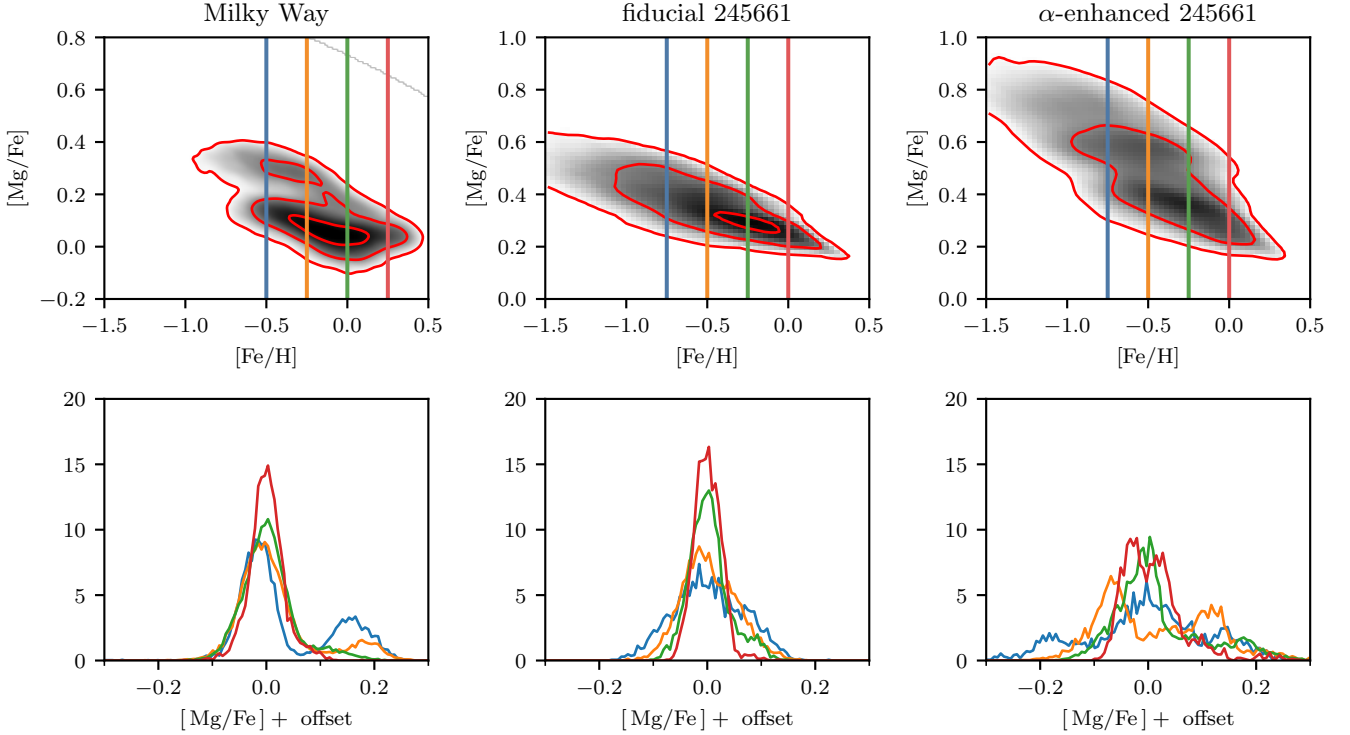


**Figure 17.** The same as Figure 1, but for a random subhalo from our catalog at  $z = 1.5$ .

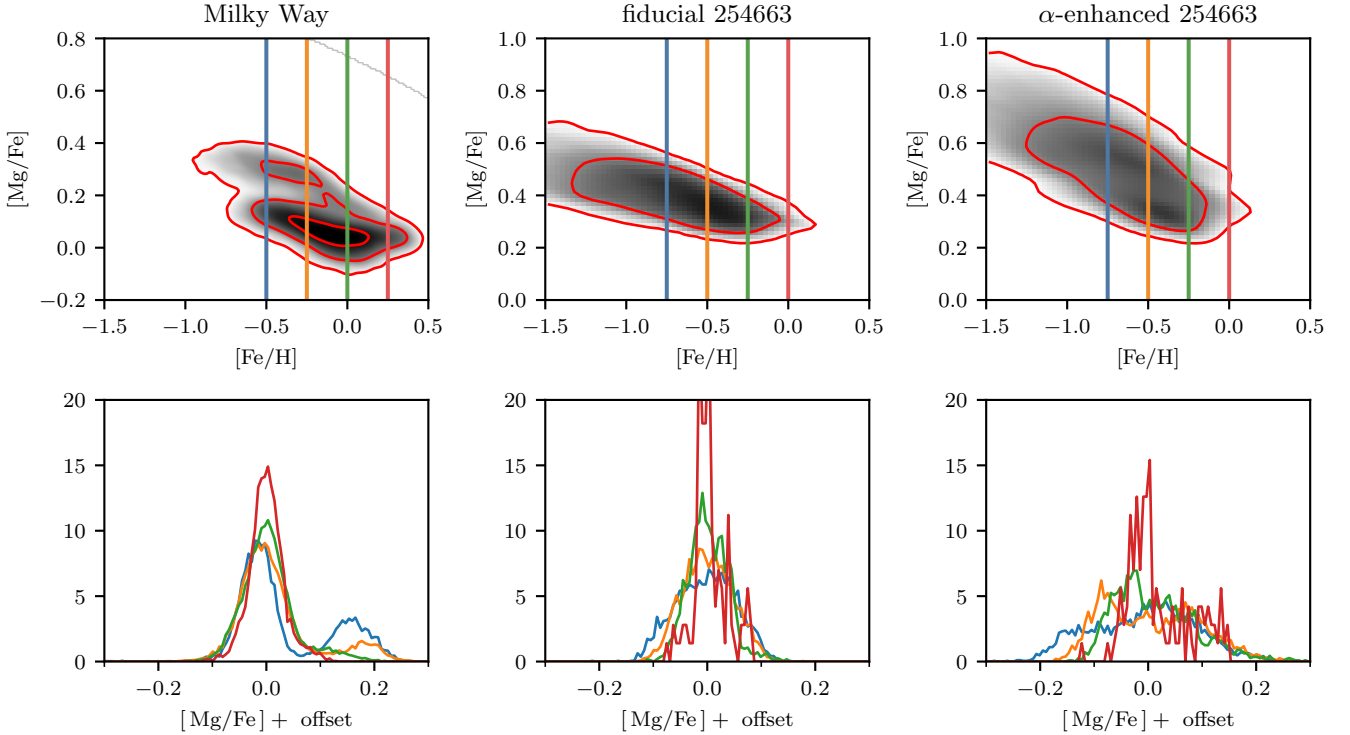


**Figure 18.** The same as Figure 1, but for a random subhalo from our catalog at  $z = 1.5$ .

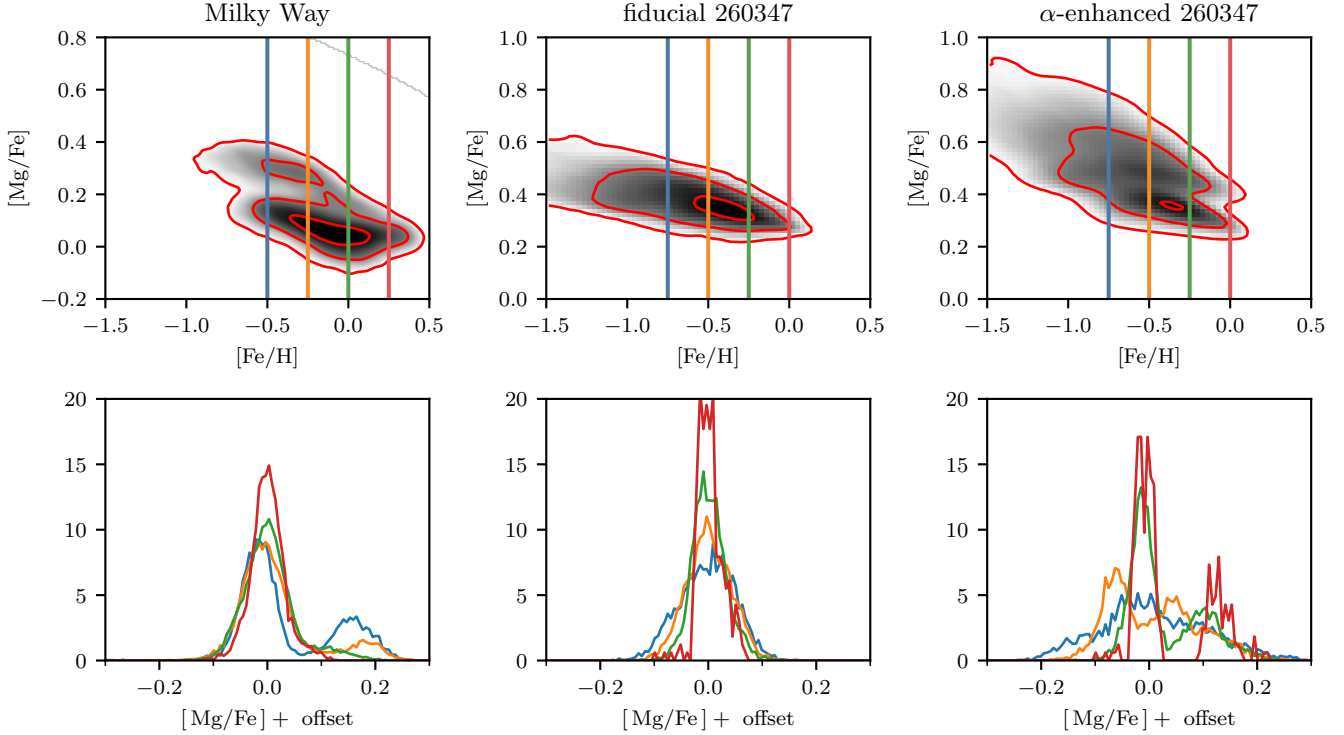


**Figure 19.** The same as Figure 1, but for a random subhalo from our catalog at  $z = 1.5$ .

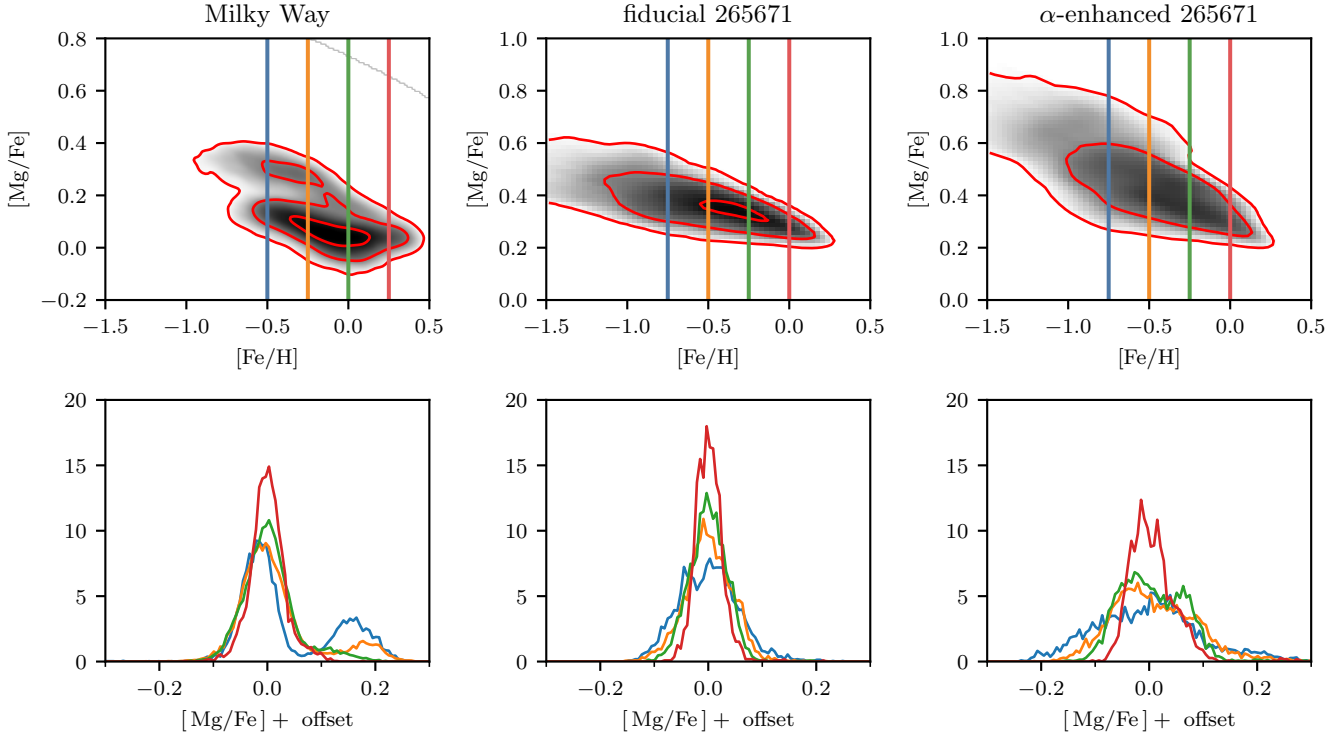


**Figure 20.** The same as Figure 1, but for a random subhalo from our catalog at  $z = 1.5$ .

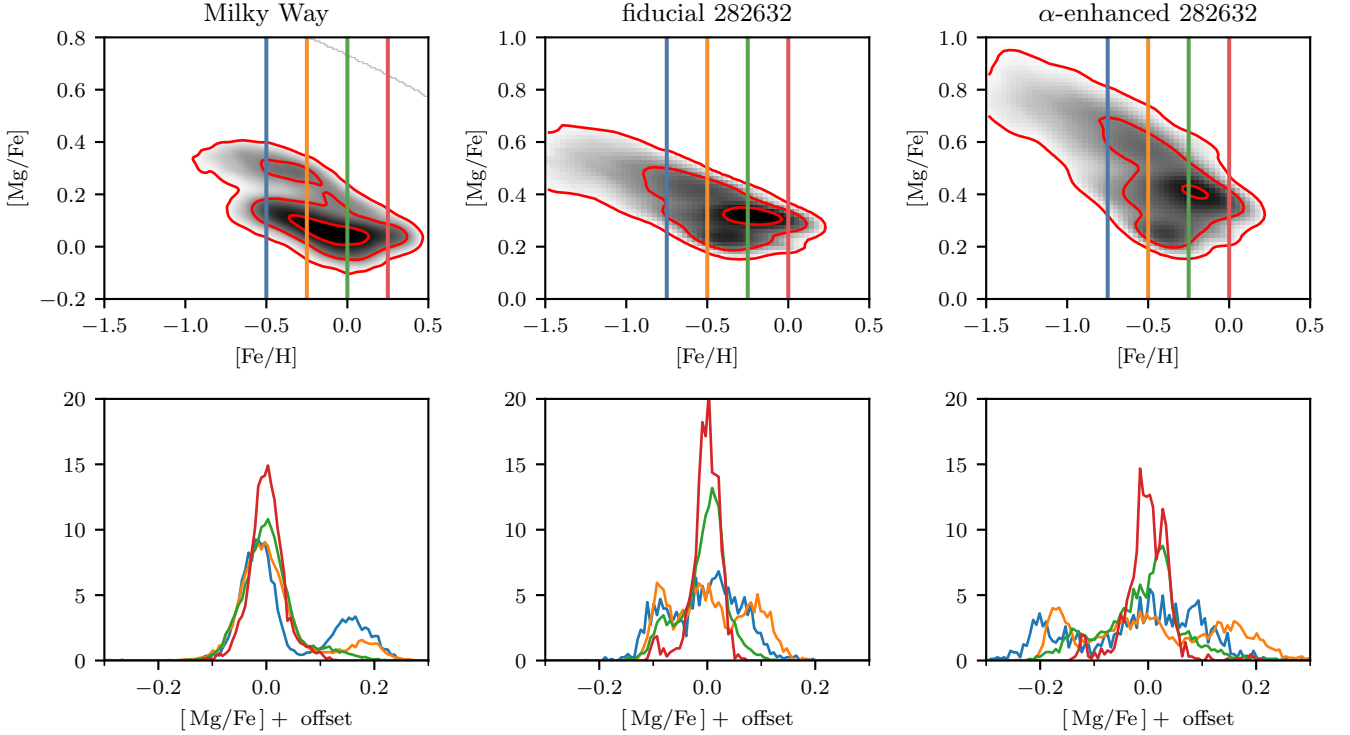


**Figure 21.** The same as Figure 1, but for a random subhalo from our catalog at  $z = 1.5$ .

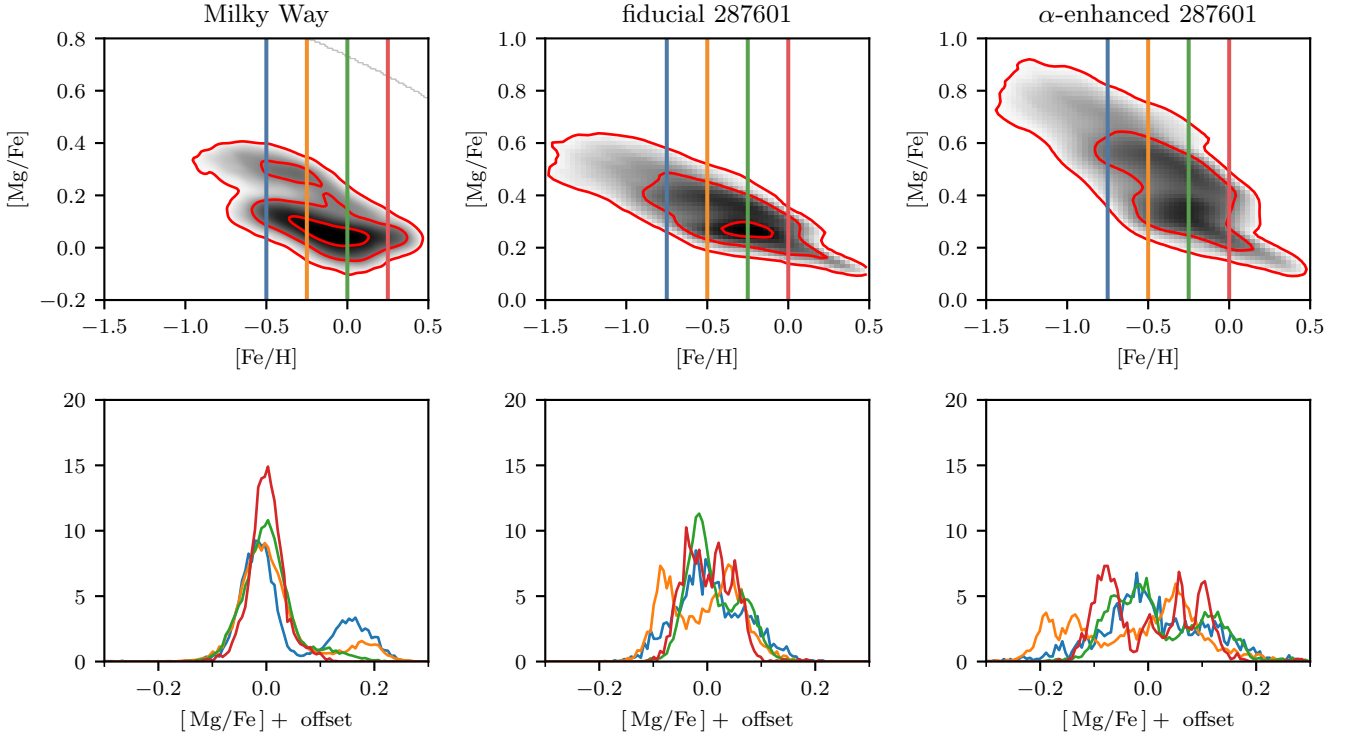


**Figure 22.** The same as Figure 1, but for a random subhalo from our catalog at  $z = 1.5$ .

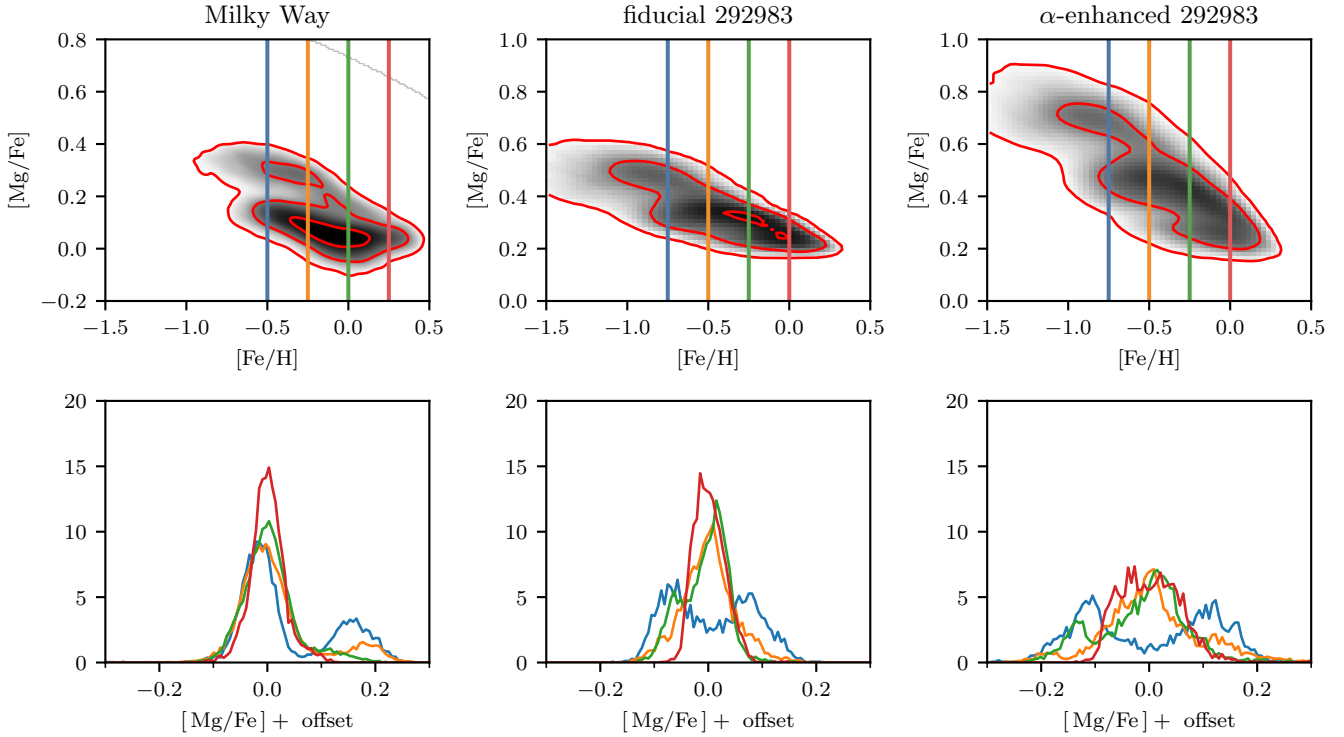


**Figure 23.** The same as Figure 1, but for a random subhalo from our catalog at  $z = 1.5$ .